SF 298 MASTER COPY KEEP THIS COPY FOR REPRODUCTION PURPOSES

REPORT DOCUMENTATION PAGE

Form Approved
OMB NO. 0704-0188

Public reporting burden for this collection of information is estimated to average 1 hour per response, including the time for reviewing instructions, searching existing data sources, gathering and maintaining the data needed, and completing and reviewing the collection of information. Send comment regarding this burden estimates or any other aspect of this collection of information, including suggestions for reducing this burden, to Washington Headquarters Services, Directorate for information Operations and Reports, 1215 Jefferson Davis Highway, Suite 1204, Arlington, VA 22202-4302, and to the Office of Management and Budget, Paperwork Reduction Project (0704-0188), Washington, DC 20503.

1. AGENCY USE ONLY *(Leave blank)*

2. REPORT DATE
21 October 1996

3. REPORT TYPE AND DATES COVERED
Final, Sept 93 - 29 Aug 96

4. TITLE AND SUBTITLE
Hierarchical Adaptive Microstructures: Smart Steels

5. FUNDING NUMBERS
DAAH04-93-G-0471

6. AUTHOR(S)
Gregory B. Olson

7. PERFORMING ORGANIZATION NAMES(S) AND ADDRESS(ES)
Northwestern University
633 North Clark Street
Evanston, IL 60208-1110

8. PERFORMING ORGANIZATION REPORT NUMBER

9. SPONSORING / MONITORING AGENCY NAME(S) AND ADDRESS(ES)
U.S. Army Research Office
P.O. Box 12211
Research Triangle Park, NC 27709-2211

10. SPONSORING / MONITORING AGENCY REPORT NUMBER
ARO 31576.1-MS

11. SUPPLEMENTARY NOTES
The views, opinions and/or findings contained in this report are those of the author(s) and should not be construed as an official Department of the Army position, policy or decision, unless so designated by other documentation.

12a. DISTRIBUTION / AVAILABILITY STATEMENT
Approved for public release; distribution unlimited.

12b. DISTRIBUTION CODE

19961125 136

13. ABSTRACT *(Maximum 200 words)*

Inspired by biomimetic concepts, a systems approach to materials design is extended to hierarchical adaptive microstructures undergoing a programmed dynamic evolution in both processing and service to achieve novel combinations of properties. Fundamental principles are developed to support rational design of (a) high-toughness ultrahigh-strength martensitic steels of interest for advanced armor and high performance gear applications, and (b) "smart composite" ferrous superalloys for damage tolerant high temperature applications in advanced tank propulsion systems. Theoretical modelling and high resolution microanalytical experiments in the martensitic alloys address control of autocatalytic coherent precipitation to achieve efficient strengthening without embrittlement, and the controlled precipitation of optimal stability metastable austenite for adaptive dilatant transformation plasticity tuned to crack-tip stress states for efficient interaction with strain localization processes in ductile fracture. Novel composite strategies address thermodynamically compatible shape-memory alloy reinforcement for pseudoelastic crack-bridge toughening of high temperature superalloys, combined with self-healing of low temperature damage by shape-memory-assisted crack rewelding at service temperatures.

14. SUBJECT TERMS
Materials Design, Hierarchical Structures, Smart Materials

15. NUMBER IF PAGES
49

16. PRICE CODE

17. SECURITY CLASSIFICATION OR REPORT	18. SECURITY CLASSIFICATION OF THIS PAGE	19. SECURITY CLASSIFICATION OF ABSTRACT	20. LIMITATION OF ABSTRACT
UNCLASSIFIED	UNCLASSIFIED	UNCLASSIFIED	UL

NSN 7540-01-280-5500

Standard Form 298 (Rev. 2-89)
Prescribed by ANSI Std. 239-18
298-102

DTIC QUALITY INSPECTED 3

HIERARCHICAL ADAPTIVE MICROSTRUCTURES: SMART STEELS

FINAL PROGRESS REPORT

G. B. OLSON

OCTOBER 21, 1996

U.S. ARMY RESEARCH OFFICE

GRANT NUMBER DAAH04-93-G-0471

NORTHWESTERN UNIVERSITY

APPROVED FOR PUBLIC RELEASE;

DISTRIBUTION UNLIMITED.

THE VIEWS, OPINIONS, AND/OR FINDINGS CONTAINED IN THIS REPORT ARE THOSE OF THE AUTHOR(S) AND SHOULD NOT BE CONSTRUED AS AN OFFICIAL DEPARTMENT OF THE ARMY POSITION, POLICY, OR DECISION, UNLESS SO DESIGNATED BY OTHER DOCUMENTATION.

Foreword: Materials as Hierarchical Systems

The late C. S. Smith [1] expounded a "systems" view of materials as hierarchical structures with properties governed by dynamic evolution in processing and in service. The Smith Philosophy has been developed into a methodology for rational design of complex materials, pioneered by the multi-institutional Steel Research Group (SRG) program centered at Northwestern University [2-4], demonstrating successful application in high toughness ultrahigh-strength alloy steels [4,5]. This view of a secondary-hardening martensitic alloy steel as a system is summarized in Figure 1 [2], depicting the hierarchy of microstructural subsystems controlling the required set of properties for desired performance, and the sequential processing subsystems which in turn control structure. Organized within this framework, basic research integrating materials science, applied mechanics and quantum physics has focused on key process/structure and structure/property relations, defining quantitative microstructural objectives expressible in thermodynamic terms (including scaling factors governing dynamic evolution), and the THERMOCALC thermochemical database and software system [6] has been applied as an integrative design tool predicting multicomponent alloy composition capable of achieving desired multiphase microstructures under prescribed processing conditions. The successful application of this approach in ultrahigh strength steels has made possible an undergraduate course in Materials Design [3], and the extension of thermodynamics-based systems design to ceramics and polymers is now being undertaken within the Department of Materials Science and Engineering at Northwestern [7].

C. S. Smith also emphasized the strong parallels between engineering materials and the hierarchical structures of the biological world [1,8]. The discovery that relatively primitive biological systems such as viruses and bacteria exploit such sophisticated materials technology as martensitic transformation plasticity and the shape memory effect [9] reinforces this parallelism. In response, an active area of current investigation is the field of biomimetics [10,11] in which complex biological systems are investigated to incorporate biological principles in the rational design of more sophisticated engineering materials. This has inspired the notion of extending materials structure to both higher levels of hierarchy and more dynamic character to achieve "adaptive" or "smart" microstructures programmed to evolve along predetermined pathways in response to a given stimulus to achieve novel properties. Such programming "brings to life" Smith's seminal vision of dynamic hierarchical materials.

The research reported here is aimed at extending the SRG systems design approach to higher levels of structural hierarchy, while incorporating more dynamic character in the form of adaptive system concepts via a synergistic integration of materials science and applied mechanics. The research addresses both the methodology of rational design at new levels of materials complexity, and the fundamental principles of specific materials behaviors necessary to support quantitative design. Research addresses adaptive multilevel microstructures in two broad areas for applications of advanced ferrous alloys:

(a) Gradient Systems with application in high performance gear technology and advanced armor, achieving novel strength/toughness combinations through control of coherent carbide precipitation in processing and tuned-stability cracktip transformation plasticity in service.

(b) Biomimetic Laminate Systems combining an oxidation resistant and high-temperature creep resistant matrix alloy with a thermodynamically compatible ductile reinforcement consisting of a shape memory alloy imparting biologically-inspired ductile-crack-bridge toughening via thermoelastic martensite pseudoelasticity at low temperatures,

and shape-memory-induced crack clamping for diffusional damage healing at high temperatures.

These areas are chosen both to represent challenging problems in hierarchical design and to respond to performance needs specific to Army applications which pose some of the most severe requirements for high performance ferrous alloys. Designed gradient systems offer the potential for a new generation of high power density gear systems exploiting the greatly increased fatigue strength of higher case hardness levels as well as the greater thermal stability of secondary hardening steels to allow both lighter weight gears and higher gear system operating temperatures desired for helicopter transmission systems. Tough high-hardness alloys offer a new generation of shatter-resistant ultrahard armor steels with higher V_{50} ballistic penetration resistance and greatly improved resistance to plastic shear localization, of particular interest for lighter aircraft armor systems and ballistically tolerant components. The especially challenging problem of the biomimetic laminates not only tests the limits of materials design, but holds promise for tank turbine applications such as the current AGT1500 which makes extensive use of ferrous superalloys. Sufficient improvement of creep-strength/ductility combinations in ferritic-based composites would allow exploitation of their superior thermal conductivity and lower thermal expansion to displace current austenitic alloys.

TABLE OF CONTENTS

Foreword i

List of Appendixes, Illustrations and Tables iv

Project Description

A. Problem Statement 1

B. Summary of Results 1

C. Publications and Technical Reports 6

D. Participating Scientific Personnel 7

Report of Inventions 7

Bibliography 8

Appendix

LIST OF APPENDIXES, ILLUSTRATIONS AND TABLES

Figure 1. System structure of secondary hardening martensitic alloy steel.

Figure 2. System structure of high power density gears.

Figure 3. Contour plots of predicted coherent M_2C precipitation driving force and coarsening rate constant for 16Co-5Ni-0.24C steels at 510C vs. Cr and Mo content. Open points denote compositions of experimental alloy series.

Figure 4. Correlation of Peak Hardness of alloys of Figure 3 with predicted coherent M_2C driving force after precipitation of paraequilibrium cementite [4].

Figure 5. Correlation of precipitation half-completion time with predicted M_2C multicomponent coarsening rate constant [4].

Figure 6. Measured composition dependence of a and c lattice parameters of $(Mo_{1-X}Cr_X)_2C$ carbides [21].

Figure 7. Computed elastic self energies vs. particle/matrix lattice parameter ratios for two shapes of coherent M_2C carbides in Fe matrix.

Figure 8. Correlation of measured hardness with Orowan-Ashby strengthening theory based on SANS data; predicted dependence of hardness at precipitation completion on alloy carbon content.

Figure 9. Toughness-hardness plot with dark bands denoting properties of transformation toughened (TT) materials; dashed box denotes original SRG objectives.

Figure 10. Dark field electron micrograph using 002_γ reflection to reveal large interlath (A) and fine (B) intralath precipitated austenite in transformation-toughened Aermet100 of Figure 9. Lower plot shows apparent Ni contents of various small B-type austenite particles using VG603 STEM microanalysis.

Figure 11. Carbon diffusivity determined from diffusion profiles in carburized Fe-20Co-10Ni, showing fit of new mobility database.

Figure 12. Comparison of measured C diffusion profiles in carburized Aermet100 steel with predictions of DICTRA simulations employing new mobility data.

Figure 13. Hardness profile obtained in C2 prototype gear steel compared with conventional EN36C gear steel.

Figure 14. System structure of self-healing "smart steel" superalloy composite.

Figure 15. Computed 4-phase α-B2-γ-γ' field in Fe-Ni-Al-Ti system at 600C based on preliminary thermodynamic database. Compositions A and B represent α-B2 and γ-γ' alloys, respectively.

Figure 16. Measured composition profiles in diffusion couple of alloys A and B reacted 24hr at 1100C. Boxes denote bulk compositions measured far from couple interface.

Figure 17. Measured diffusion composition trajectories in A-B couples projected on median Ti plane in (a) and median Al plane in (b). Corresponding DICTRA simulations for γ single-phase A1/B and α-γ two-phase A2/B couples in (c) and (d).

Figure 18. Electron micrographs of alloy A after aging 1 week at 600C; (a) bright field image of large γ particles in fine α-B2 matrix; (b) higher magnification dark field image using 100 B2 super-lattice reflection to reveal fine B2 dispersion in α.

APPENDIX - "Austenite Stability and Mechanical Properties of Austempered Ductile Iron," D. Bergstrom, doctoral research, Northwestern University.

Research Progress

A. Problem Statement

While quantitative property objectives are important to obtain sufficient focus of basic research coordinated within an interdisciplinary systems design framework, the primary objectives of this research effort are the fundamental principles and basic data necessary to support rational design. This includes the principles of microstructural evolution during coherent carbide precipitation for efficient strengthening without embrittlement, the control of metastable austenite precipitation for optimal-stability transformation toughening, the behavior of pseudoelastic crack-bridge toughening, and the shape-memory-based healing of internal composite damage. The research emphasizes the dynamics of microstructural evolution in processing and in service, and the design methodology for control of multilevel dynamic hierarchical microstructures as programmed adaptive systems.

Specific property targets which guide the conceptual design of prototype materials for evaluation are a case hardness of R_c70 for the secondary hardening gear steels, offering the potential for a 60 pct. increase in contact fatigue strength. Desired core properties should maintain a K_{IC} toughness of >60 MPa$\sqrt{m}$ at R_c50 hardness to provide a critical flaw size superior to current aerospace gear steels, while maintaining thermal stability up to 400C. Armor steel objectives are a transformation toughened secondary hardening steel of R_c57 hardness with $K_{IC} > 80$ MPa$\sqrt{m}$ for shatter resistance. Specific operating temperature requirements for the shape-memory reinforced superalloy laminates would be 600-700C with a 10^5hr creep strength of 100 MPa.

B. Summary of Results

B.1 Gradient Systems

The system structure of Figure 2 represents our long-term goal in expanding our approach to high power density gear systems to higher levels of structural hierarchy. The approach considers not only the case/core gradient system of the gear steel itself, but the integrated design of compatible surface hard coatings and associated interfaces, ultimately incorporating design of gear shape to optimally exploit new material properties. Also represented are alternative processing routes to provide cost-effective manufacturing strategies for specific application areas. Research thus far has addressed the conventional forging and machining route appropriate to military helicopters, focussing on the case/core gear steel subsystem.

Before further discussion of the gradient gear steel, we next examine the underlying phenomena allowing the desired control of strength and toughness in such systems.

a) Strengthening

The first dynamic problem of interest in the systems of Figures 1 and 2 is the evolution of coherent carbide precipitation controlling strength. The pioneering work of Speich [12] established that good toughness in secondary hardening alloy steels demands near-completion of M_2C alloy carbide precipitation in order to dissolve transient cementite (Fe_3C) particles that otherwise contribute to microvoid nucleation during ductile fracture. The challenge to maintaining strength in such an overaged condition is to maintain a fine carbide particle size. A thorough electron microscopy study of M_2C precipitation in the commercial AF1410 steel [13] was performed in the doctoral research of J. S. Montgomery (now at ARL/MD) in conjunction with Small-Angle Neutron Scattering (SANS) studies by Weertman and coworkers [14],

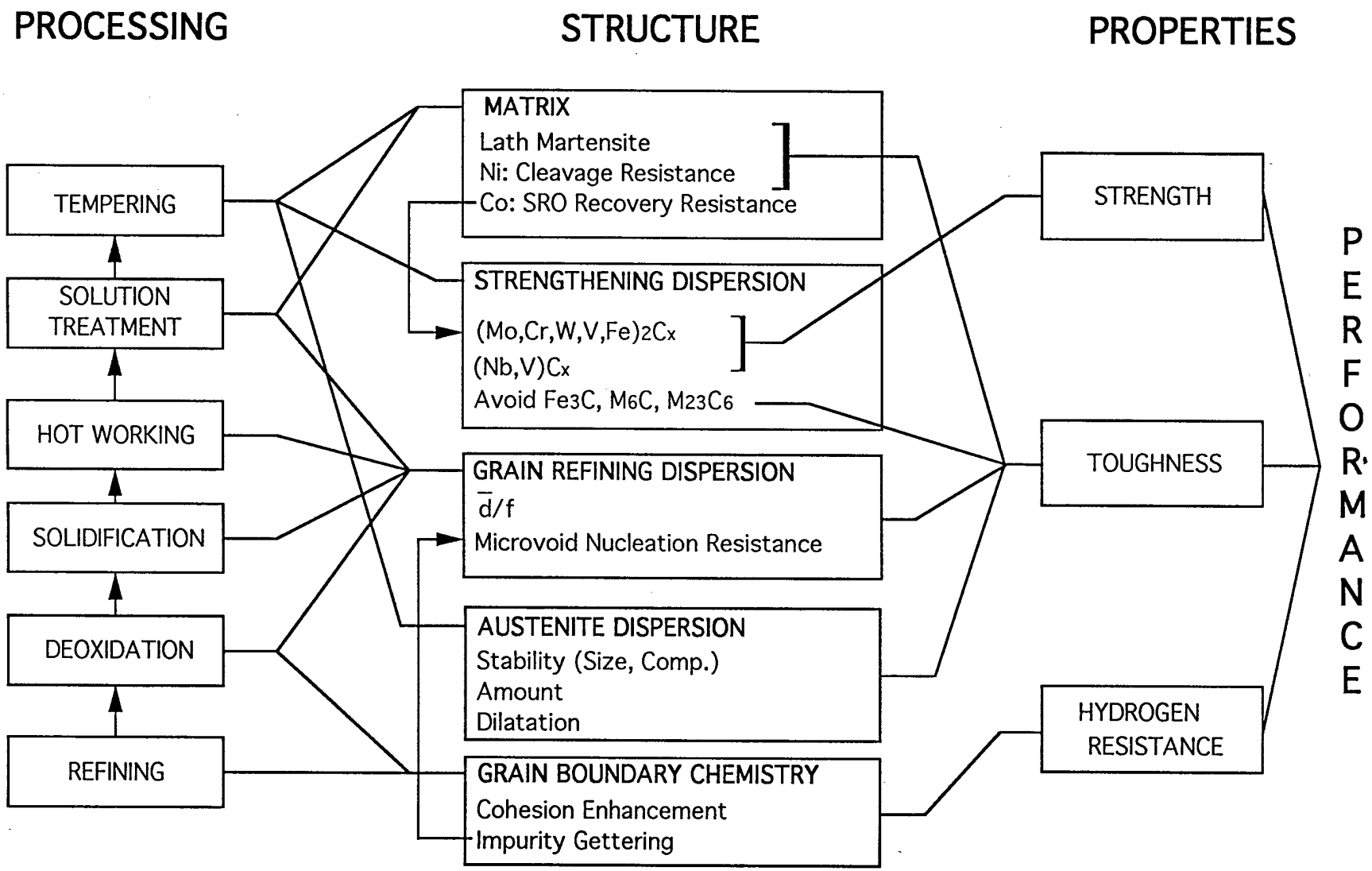

Figure 1. System structure of secondary hardening martensitic alloy steel.

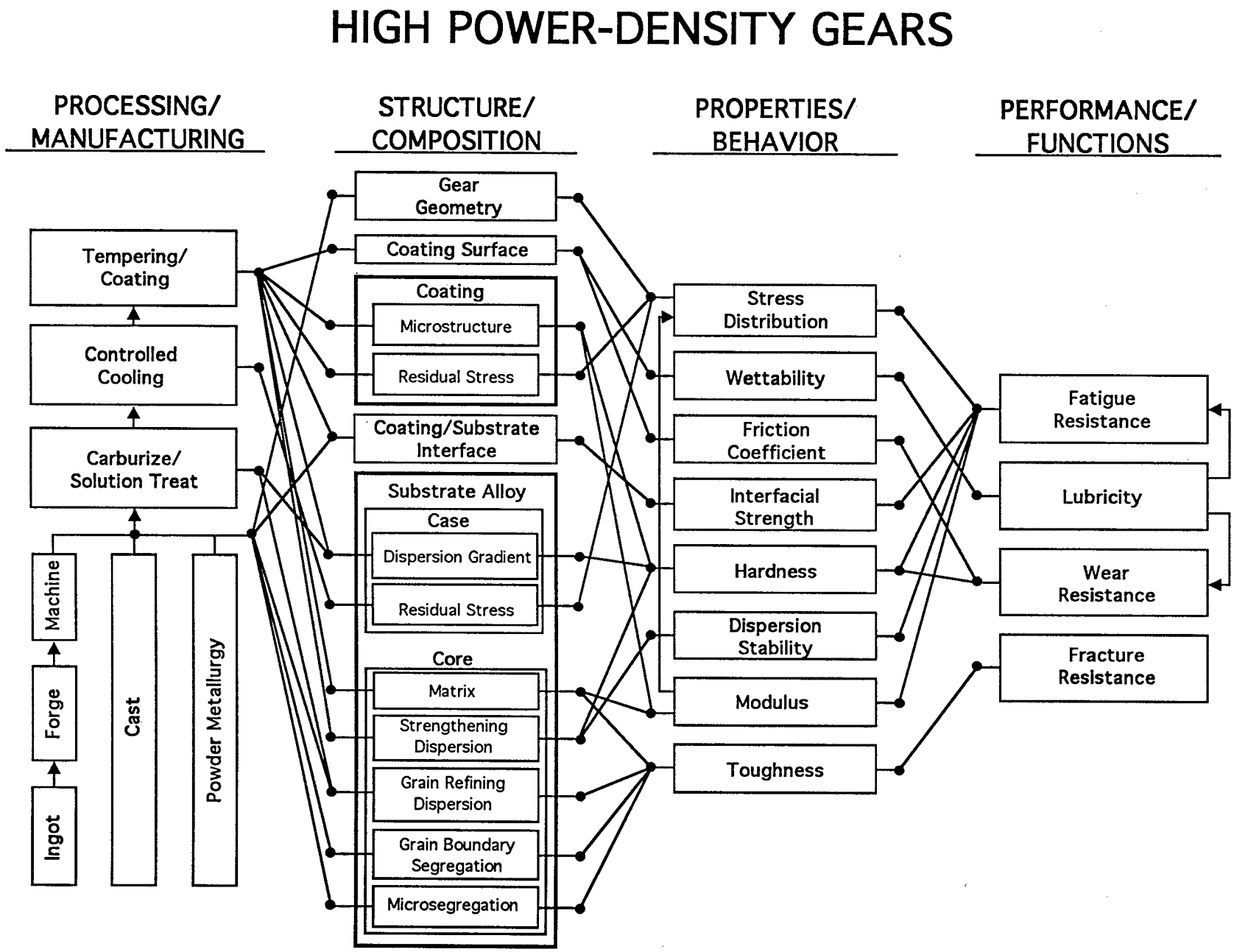

Figure 2. System structure of high power density gears.

demonstrating coherent precipitation behavior consistent with recent theory of precipitation at high supersaturations [15,16]. In this regime the fundamental scaling factor governing particle size (and thus alloy strength) is the initial critical nucleus size which scales inversely with the thermodynamic driving force for precipitation; the time scale of precipitation is governed by a diffusion time defined by the coarsening rate constant. To compute the thermodynamic driving force for coherent M_2C precipitation, the doctoral research of K. C. King with Professors T. Mura and P. Voorhees addressed the elastic self energy of the coherent carbides [17], and also explored the elastic interactions with dislocations during heterogeneous nucleation [18]. Incorporating the composition dependence of the carbide lattice parameters, the THERMOCALC chemical thermodynamic database was then modified to incorporate the additional elastic self energy contribution to the thermodynamics of coherent precipitation. To control the time scale of precipitation, theories of coarsening kinetics in multicomponent systems were developed by Kuehmann & Voorhees [19] and Umantsev [20] to define a multicomponent diffusional rate constant.

Our more recent work has tested model predictions in a series of 16Co-5Ni-0.24C steels with the Cr and Mo contents represented in Figure 3 displaying contour plots of predicted coherent precipitation driving forces and coarsening rate constants. An X-ray diffraction study of the precipitation hardening behavior of these alloys was initiated by Visiting Scientist S. Endo of NKK Japan and correlated with model predictions by Research Scientist C. J. Kuehmann [4]. Measured peak hardness shows a strong correlation with the coherent precipitation driving force, Figure 4, after taking into account the "paraequilibrium" condition of prior precipitation of cementite under carbon diffusion control. Figure 5 shows a good correlation of the measured precipitation half time and the predicted multicomponent coarsening rate constant calculated for a condition of 50% relative supersaturation. The models thus provide the basis for thermodynamic prediction of strengthening and precipitation rate with useful accuracy.

Toward improved precision of the M_2C coherent thermodynamics, the recently completed doctoral research of C. Knepfler [21], with ceramist Prof. K. Faber, has addressed the synthesis and characterization of $(Mo,Cr,V,Fe)_2C$ carbides in bulk form, measuring the composition dependence of lattice parameters, thermal expansion and isotropic elastic moduli as inputs into a more precise treatment of the composition and temperature dependence of the carbide elastic self energy. Measured lattice parameters of the $(Mo,Cr)_2C$ system are summarized in Figure 6. Measured elastic constants were also applied to an analysis of the critical particle size for the shear/bypass transition in precipitation strengthening of steels, and carbide heat capacity vs. temperature was measured defining Debye temperatures for a more precise description of the M_2C chemical thermodynamics.

The doctoral research of R-H. Liarng with Prof. Mura has incorporated Knepfler's measurements in refined calculations of the carbide elastic self energy in an iron-based matrix, taking into account the differing elastic constants of matrix and particle, and the role of particle shape. Figure 7 depicts computed elastic self energies vs. particle/matrix lattice parameter ratios for two particle shapes (prolate spheroids of aspect ratio 1 and 3) using typical values of the carbide shear modulus. Liarng also computed internal stresses on carbide shear systems relevant to coherency loss mechanisms, predicted solute distributions around coherent particles, and considered interparticle elastic interactions promoting autocatalytic nucleation. As the transformation eigenstrains for a coherent M_2C carbide in an Fe matrix are quite high, these linear elastic calculations are regarded as upper bound estimates of self energies and local stresses. To rationalize observed coherent nucleation conditions and coherent particle compositions measured by atom-probe microanalysis, it has been necessary to apply a correction factor of 1/3 to the computed self energies. Liarng has performed lower bound self energy estimates by excluding the energy density contributions of highly strained regions likely to be

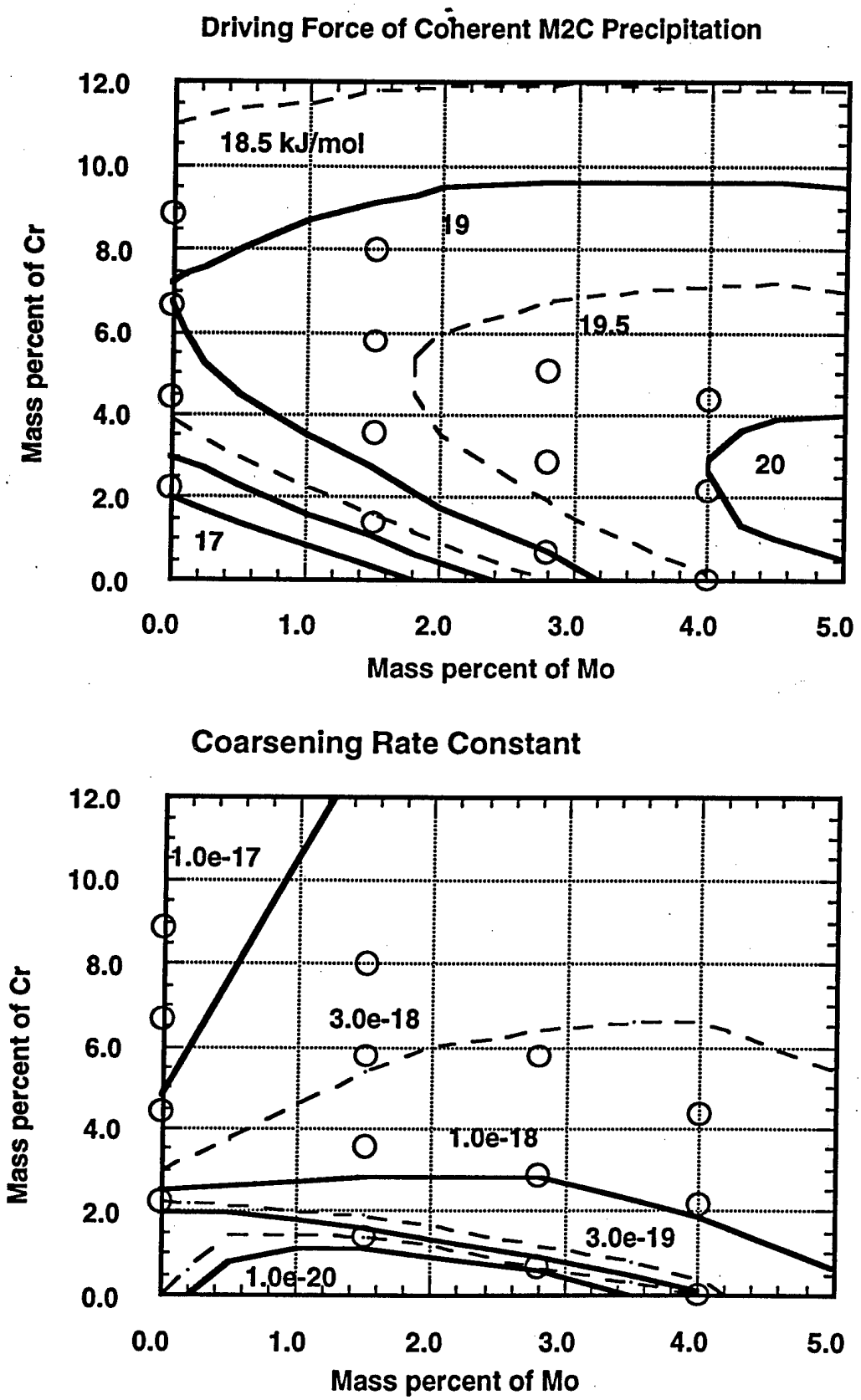

Figure 3. Contour plots of predicted coherent M_2C precipitation driving force and coarsening rate constant for 16Co-5Ni-0.24C steels at 510C vs. Cr and Mo content. Open points denote compositions of experimental alloy series.

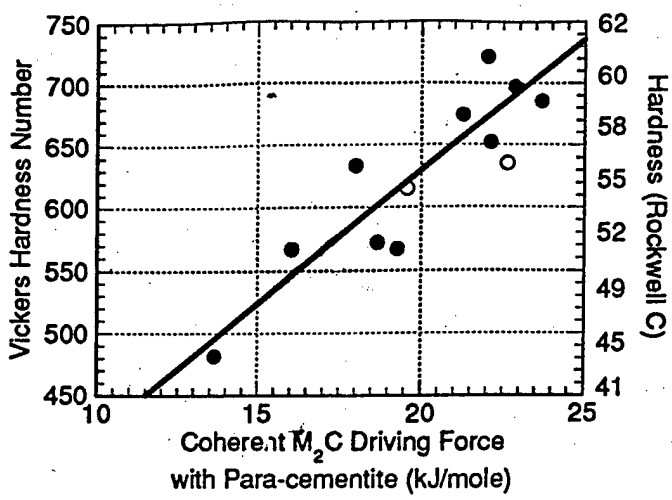

Figure 4. Correlation of Peak Hardness of alloys of Figure 3 with predicted coherent M_2C driving force after precipitation of paraequilibrium cementite [4].

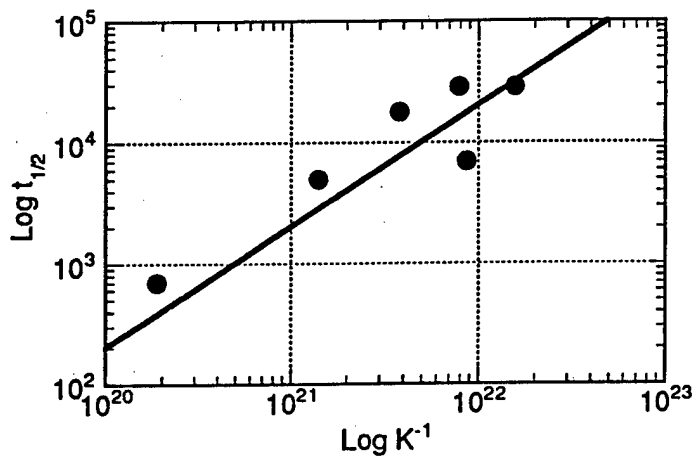

Figure 5. Correlation of precipitation half-completion time with predicted M_2C multicomponent coarsening rate constant [4].

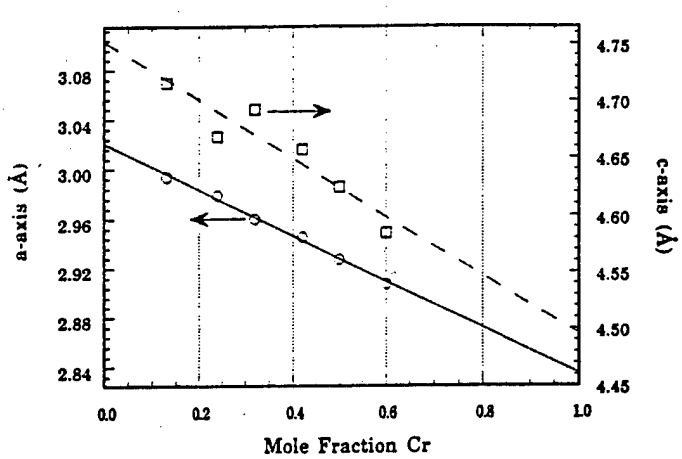

Figure 6. Measured composition dependence of a and c lattice parameters of $(Mo_{1-X}\ Cr_X)_2C$ carbides [21].

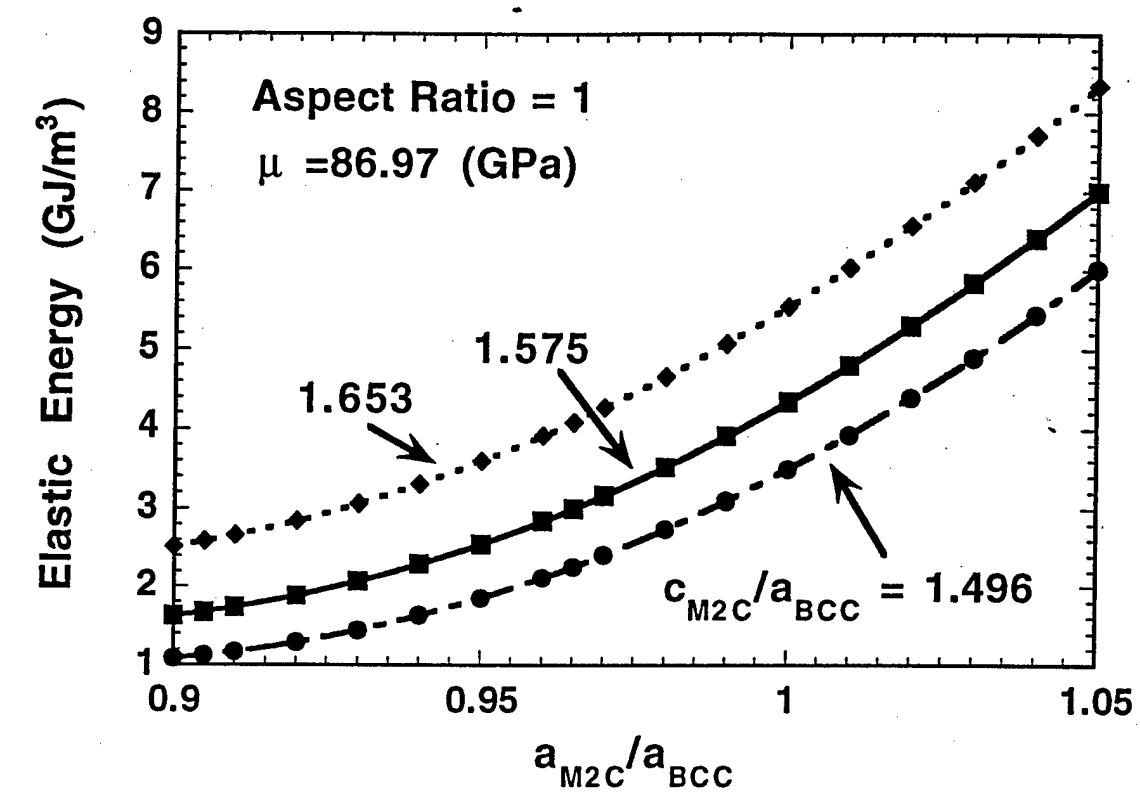

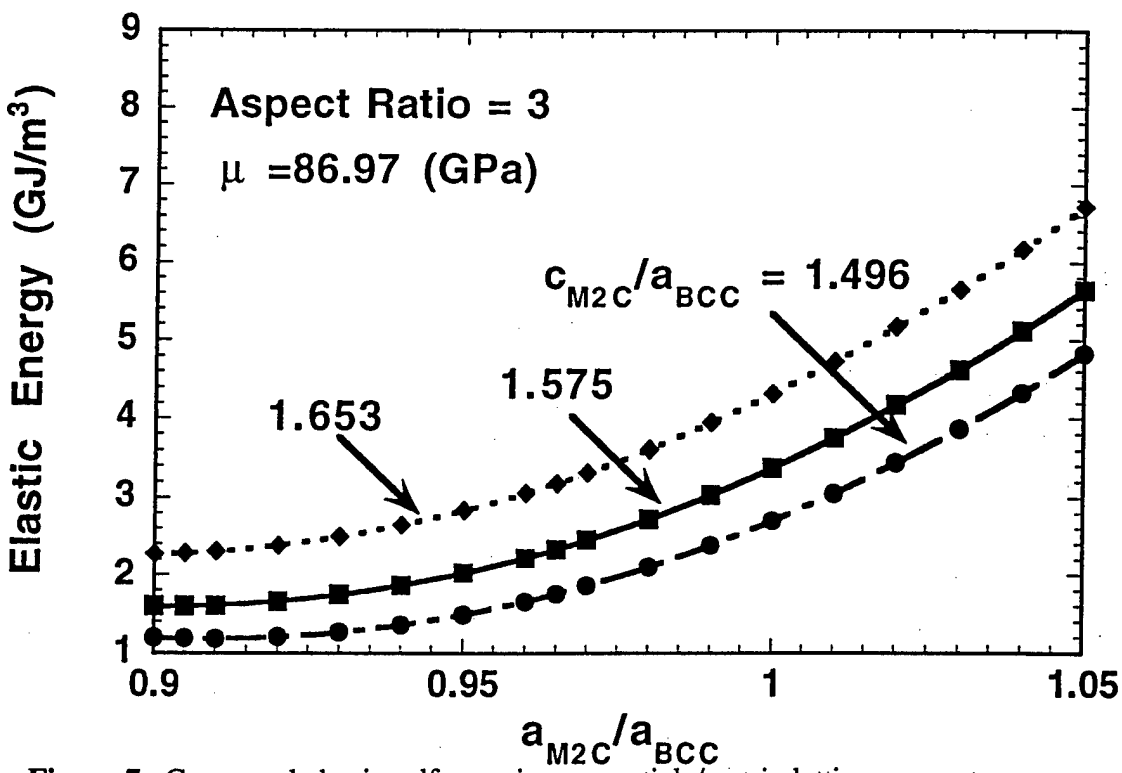

Figure 7. Computed elastic self energies vs. particle/matrix lattice parameter ratios for two shapes of coherent M_2C carbides in Fe matrix.

strongly nonlinear, similar to the dislocation core cutoff approximation, supporting correction factors of this magnitude.

Employing the more precise coherent thermodynamics provided by the improved elastic self energy estimates, the correlation of strength and thermodynamic driving force in Figure 4 can be modeled more precisely be relating driving force to particle size, and particle size to strength. The latter has been treated as part of the doctoral research of J. Wise. Figure 8 depicts the correlation of measured hardness with the Orowan-Ashby dislocation bypass strengthening equation for particles of radius R and mean spacing L, using a dislocation core size of r_o=b. The fit is based on the SANS data so far available for three of the 0.24C alloys in the series of Figure 3. The lower figure then predicts the dependence of hardness at completion of precipitation on alloy carbon content for various particle diameters, including the critical size d_c for the shear/bypass transition corresponding to a theoretical upper limit of strength. The trends are in good agreement with measured hardness and particle size in commercial and experimental alloys investigated.

b) Toughening

Early work under the SRG Program addressed toughening of UHS steels via (a) control of microvoid nucleating particle dispersions governing plastic shear localization [22-25], and (b) dispersed-phase transformation toughening by precipitation of optimal stability austenite particles [26,27]. A continuing effort under ONR support has defined requirement to resist intergranular fracture [28]. Guided by model predictions on microvoiding behavior, the recent doctoral research of C. J. Kuehmann under ARO support addressed optimization of the solution treatment of the commercial Aermet100 alloy to obtain a residual grain refining dispersion of fine TiC particles with improved resistance to microvoiding as attested by J_{IC} toughness measurements [29]. Kuehmann then explored optimization of multistep tempering treatments to achieve dispersed-phase transformation toughening in this alloy.

Our understanding of transformation toughening mechanisms has benefited from a parallel DOE-sponsored effort studying fully austenitic alloys, experimentally demonstrating the role of phase stability and dilatation [2,30-32] with numerical simulations defining the effect of transformation plasticity in enhanced resistance to plastic localization [33] and microvoiding processes [34]. ARO sponsored research has explored the application of this understanding to the control of dispersed-phase transformation plasticity in the secondary hardening martensitic steels. Our progress is summarized by the toughness-hardness plot of Figure 9. Early experiments guided by thermodynamic predictions of achievable austenite stability in the AF1410 composition boosted toughness to the AF1410-TT band employing multistep tempering to nucleate a fine dispersion of Ni enriched austenite while maintaining a sufficiently fine carbide dispersion for desired strength [26]. Our efforts to apply the same strategy to the higher strength Aermet100 alloy revealed a much tighter processing window due to the faster carbide precipitation kinetics associated with this higher Cr composition. Initial multistep tempering studies by Kuehmann [29] demonstrated transformation toughening, but at less than desired strength levels. A more thorough study was then undertaken by Visiting Scientist M. Srinivas from the Defence Metallurgical Research Laboratory, India, establishing first the detailed low temperature tempering kinetics for optimal strengthening, then interposing short intermediate temperature austenite nucleation treatments. Detailed measurement of toughness evolution was provided by relatively simple cracktip stretch-zone measurements followed by verification of promising treatments with J_{IC} tests. The results of optimal processing are represented by the Aermet100-TT and MTL1-TT band in Figure 9. These exceptional properties were obtained with both the Aermet100 composition and our V modified lower C prototype armor steel designated MTL1. The outstanding toughness and hardness combinations are seen to lie within the dashed box representing the original property objectives of the SRG program.

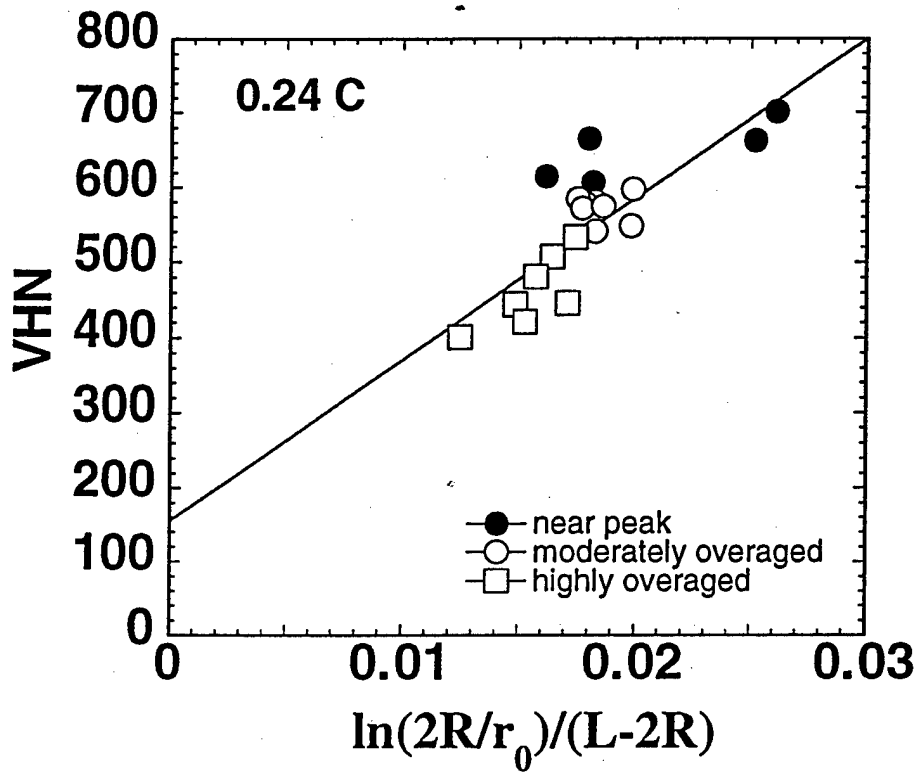

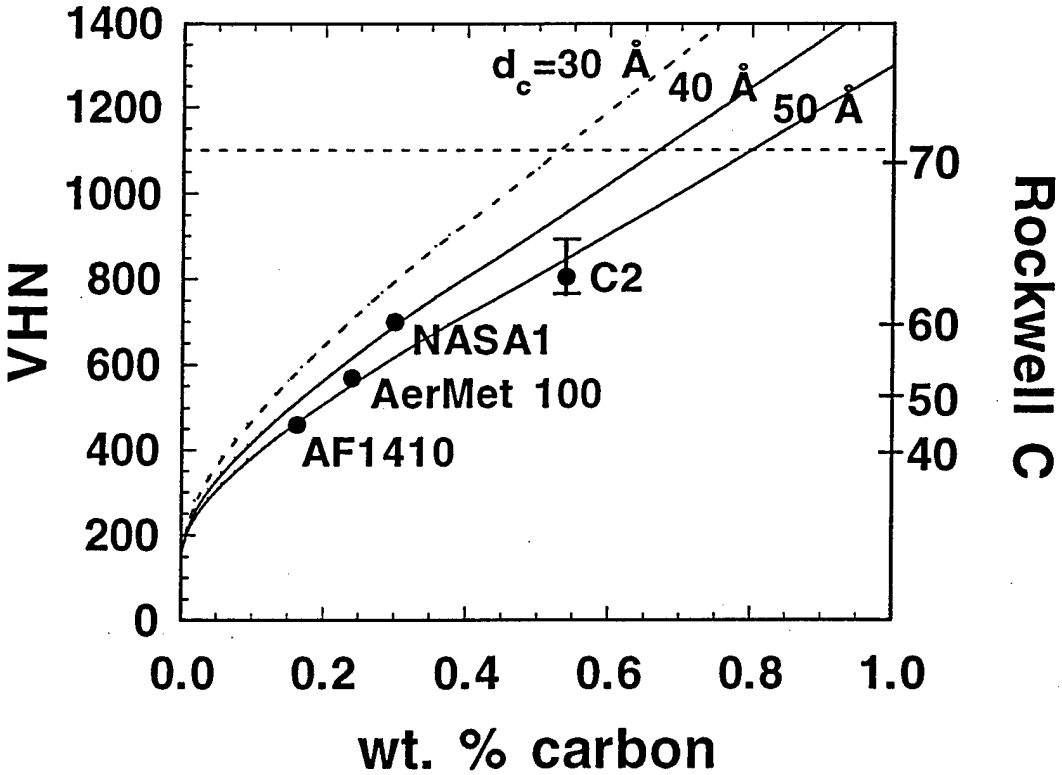

Figure 8. Correlation of measured hardness with Orowan-Ashby strengthening theory based on SANS data; predicted dependence of hardness at precipitation completion on alloy carbon content.

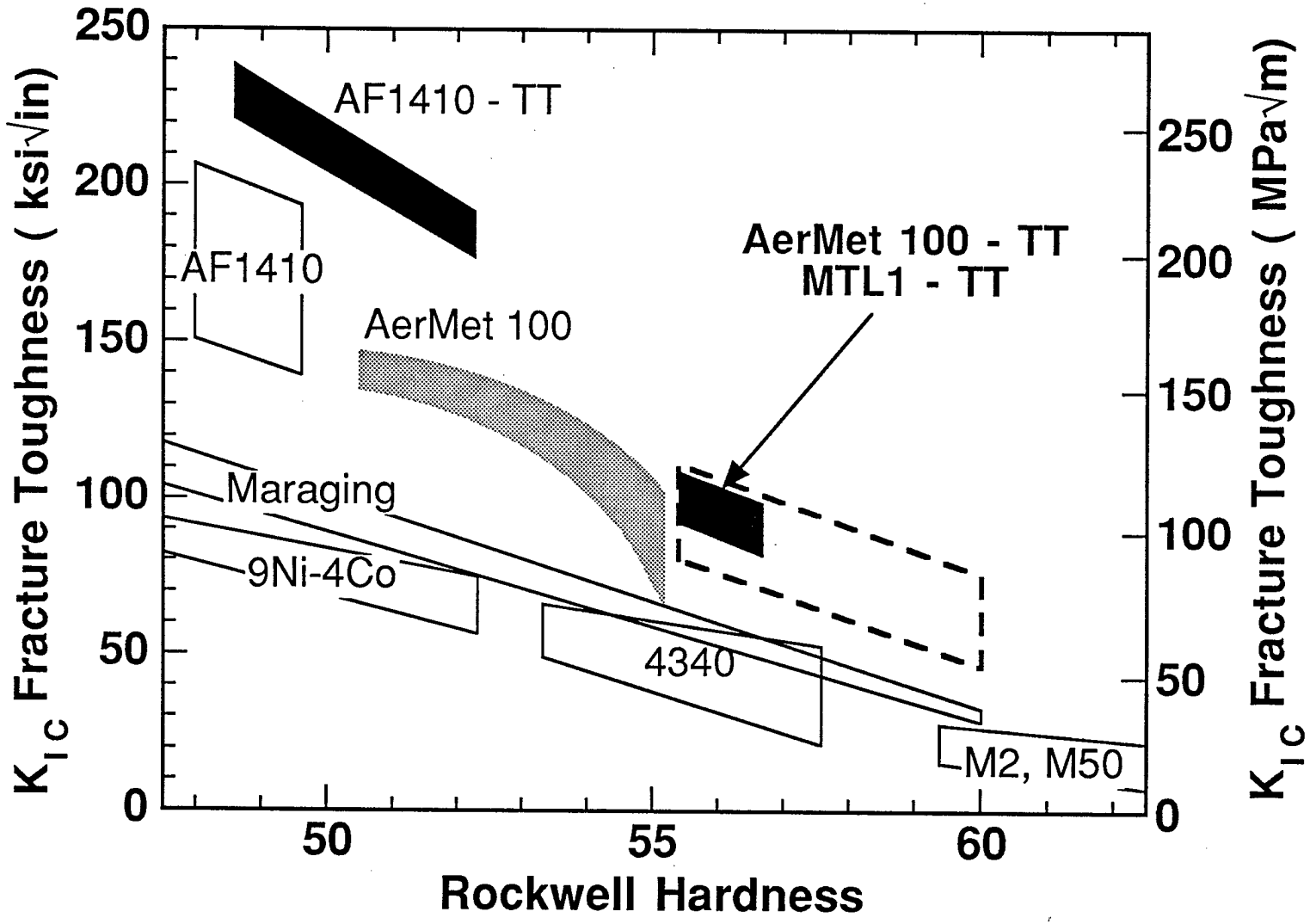

Figure 9. Toughness-hardness plot with dark bands denoting properties of transformation toughened (TT) materials; dashed box denotes original SRG objectives.

Austenite precipitation behavior in these alloys is being investigated by electron microscopy and microanalysis in the doctoral research of fellowship student H. Lippard cosupervised by Prof. V. Dravid. The dark-field micrograph of Figure 10 (using an 002_γ reflection) reveals two forms of precipitated austenite in the Aermet100-TT material of Figure 9. The microstructure is similar to our previous observations in AF1410-TT [26] in which slightly Ni enriched austenite discs at martensite lath boundaries (A) coexist with a fine dispersion of more Ni rich intralath precipitates (B); the lath boundary precipitation gives nonequilibrium austenite compositions while the composition of the fine intralath precipitates is in good agreement with equilibrium predictions. The high austenite stability responsible for toughening these UHS steels is attributed to the fine size and Ni enrichment of the latter. While the fine austenite in AF1410-TT had a particle size of 20nm, the fine particles of Figure 10 observed in Aermet100-TT are only 5nm, taxing the limits of high resolution electron microanalysis. In addition to the 200kV cold field emission Hitachi HF2000 analytical electron microscope at Northwestern, the samples have been analyzed with a Phillips CM20 at Gatan Laboratories (employing a Gatan Imaging Filter for EELS imaging with the Ni core loss L-edge) and the highest brightness 300kV cold field emission UHV VG603 STEM at Lehigh University. The apparent Ni enrichments of embedded austenite particles plotted in Figure 10 were obtained with the latter instrument, supporting the interpretation of the 5nm particles as austenite, but not allowing direct composition measurement due to extreme matrix overlap at ~100nm foil thickness.

c) Gradient Systems: Gear Steels

Case hardenable secondary hardening steels for the high power density gear systems of Figure 2 may represent the most promising area for application of the design models we are developing. This line of research originated as conceptual designs in Materials Design class projects performed in collaboration with a mechanical engineering design class who identified property objectives for a 50% weight reduction in gears. Preliminary designs comparing low temperature nitriding and high temperature carburizing led to selection of carburizing as the most promising processing route to achieve the 1mm-scale case depths needed in typical gear applications. Two generations of carburizable prototype compositions were designed and evaluated. An undergraduate project evaluating the second prototype alloy, designated C2, won 1st prize in the last TMS-AIME national student design competition [35].

Research on carburizable gradient systems for gear applications has continued in the doctoral research of J. Wise, initiated under seed funding from the Ford Motor Company. Precise treatment of the dynamics of gradient formation by carburizing has been made possible by the new DICTRA multicomponent diffusion code developed at the Royal Institute of Technology in Stockholm as an extension of the THERMOCALC system. The DICTRA system combines the thermodynamic database of THERMOCALC with a mobility database to compute the full multicomponent diffusivity matrix, and solves 1, 2, and 3 dimensional diffusion problems by a finite difference method. To apply the code to carburization of the complex multicomponent steels of interest, Wise conducted preliminary carburizing experiments on an Fe20Co10Ni alloy and determined the composition-dependent C diffusivity from measured C profiles, as summarized in Figure 11. Based on these measurements, it was found necessary to modify the DICTRA mobility database (mob4) through a Co-C interaction term to give the improved fit shown in the figure. The model was then validated by comparison with measured diffusion profiles in carburized Aermet100 steel as shown in Figure 12, demonstrating excellent agreement. Combining DICTRA diffusion simulations with the strengthening model of Figure 8 provides the basis for precise control of hardness profiles in these secondary hardening steels. The hardness profile so far obtained in the C2 prototype gear steel is compared in Figure 13 with that of a conventional gear steel. Maintaining an equivalent gradient depth, a substantial

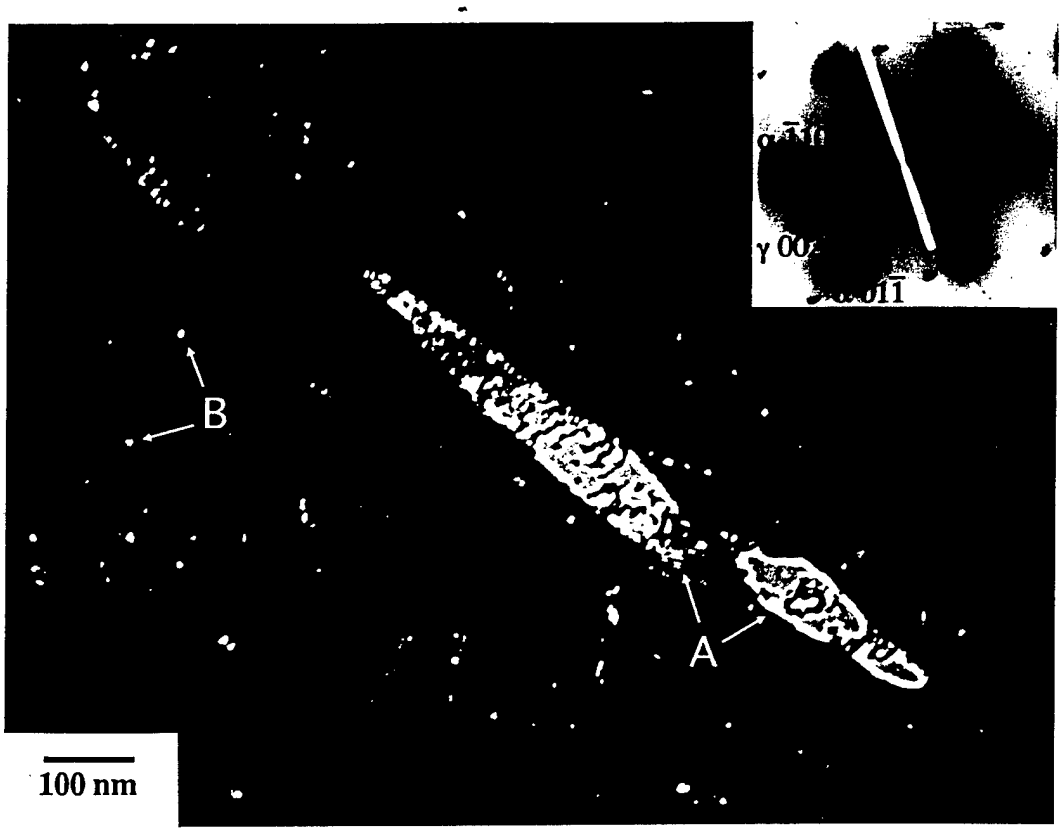

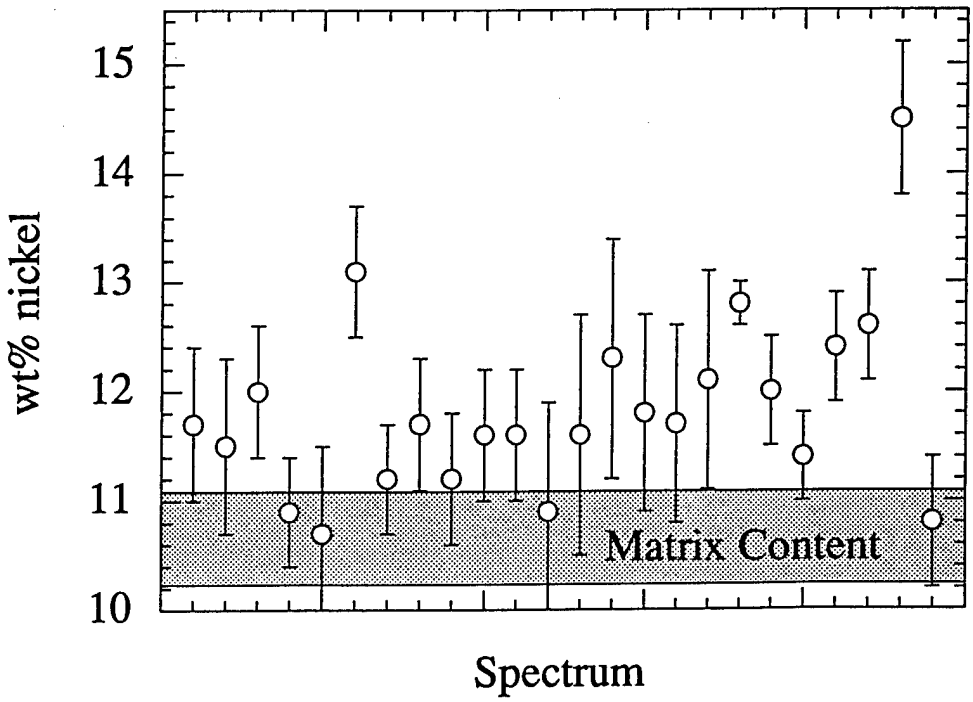

Figure 10. Dark field electron micrograph using 002_γ reflection to reveal large interlath (A) and fine (B) intralath precipitated austenite in transformation-toughened Aermet100 of Figure 9. Lower plot shows apparent Ni contents of various small B-type austenite particles using VG603 STEM microanalysis.

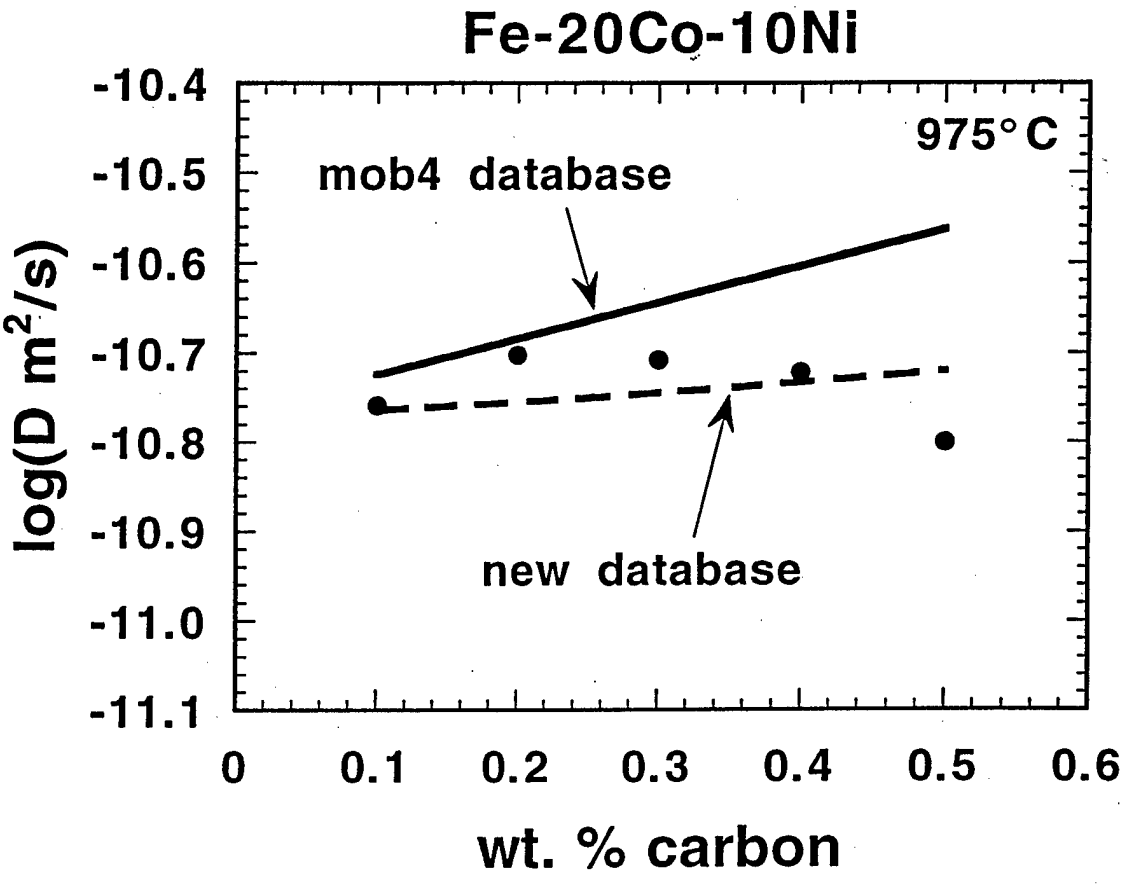

Figure 11. Carbon diffusivity determined from diffusion profiles in carburized Fe-20Co-10Ni, showing fit of new mobility database.

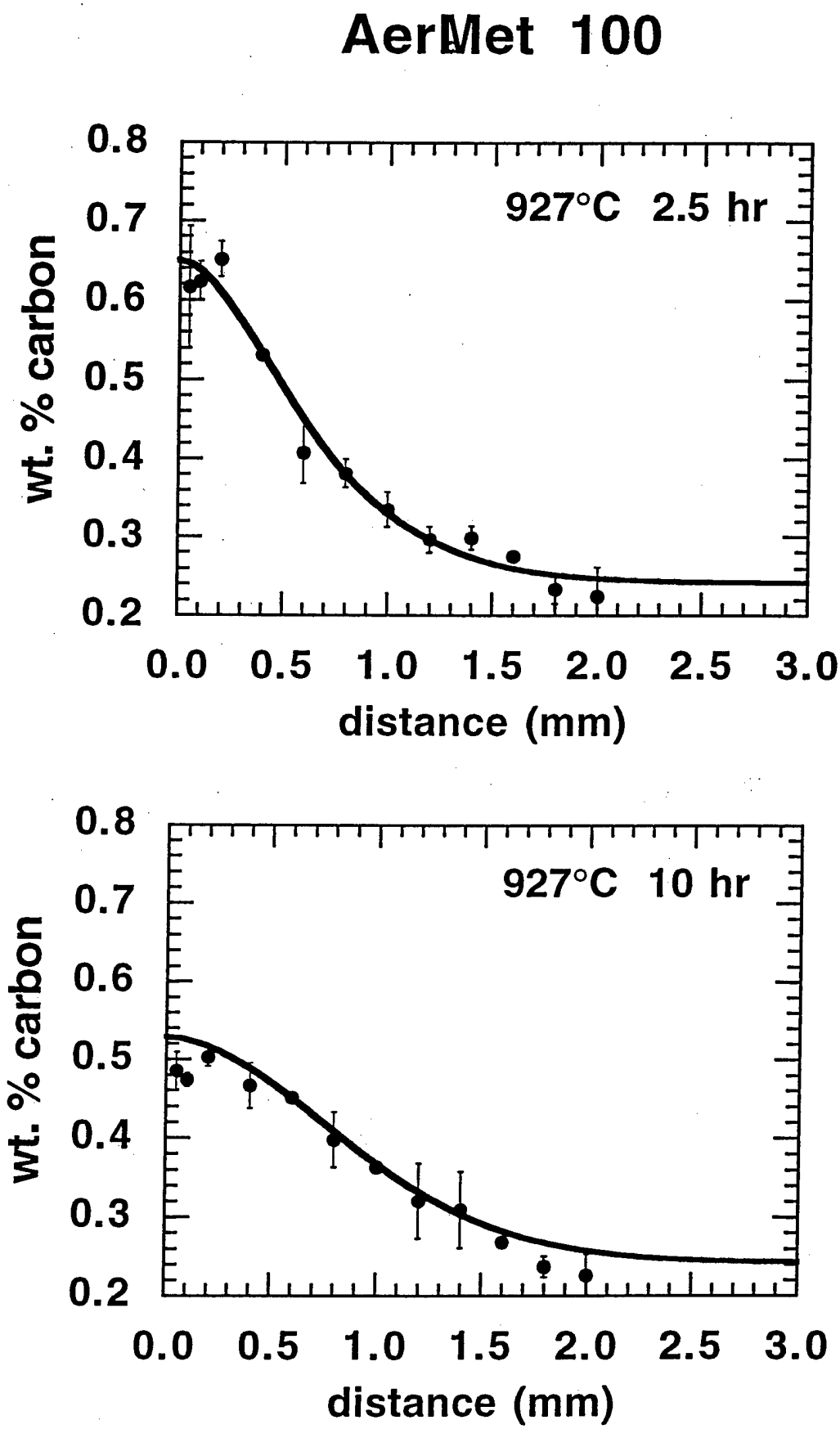

Figure 12. Comparison of measured C diffusion profiles in carburized Aermet100 steel with predictions of DICTRA simulations employing new mobility data.

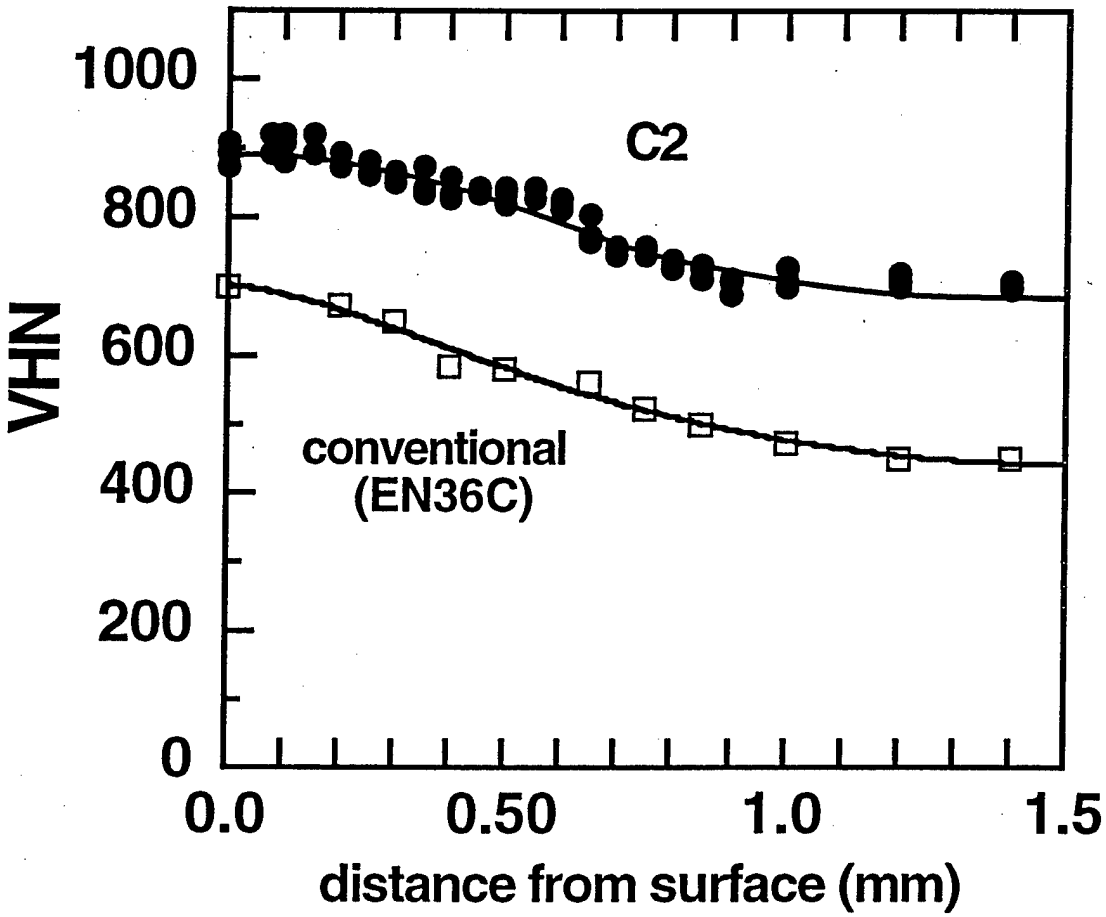

Figure 13. Hardness profile obtained in C2 prototype gear steel compared with conventional EN36C gear steel.

increment of hardness improvement has been demonstrated with a surface carbon content of 0.55C as also denoted in Figure 8.

d) High Hardness Armor Steels

Under a one-year contract from ARL/MD, formerly MTL, available SRG design tools were applied to the design of a prototype high hardness armor steel. This led to the alloy designated MTL1 in Figure 9, which was evaluated in the Masters thesis of J. Cho [29]. Employing a V addition to enhance strengthening efficiency, the alloy demonstrated properties equivalent to the Aermet100 alloy, but with lower C content (0.21C). Ballistic testing at ARL/MD demonstrated V_{50} levels at fixed plate thickness equivalent to the best monolithic armor steels. A higher carbon composition (0.25C) for higher hardness has been prepared for further evaluation at ARL/MD.

B.2 Biomimetic Laminates

Testing the limits of complexity in rational materials design incorporating biomimetic adaptive system concepts, the essential concepts of the self healing "smart steel" superalloy composite are summarized in the system chart of Figure 14. A ferritic (BCC) superalloy strengthened by a coherent dispersion of ordered B2 precipitates is reinforced by a thermodynamically compatible γ' strengthened austenitic (FCC) shape memory alloy in a laminate formed by hot rolling of a consolidated blend of prealloyed powders. The composite integrates two biomimetic concepts. At low temperatures the shape memory alloy reinforcement toughens the otherwise brittle ferritic alloy by bridging cracks via martensitic pseudoelasticity, mimicking the nonlinear polymer reinforcement of a brittle ceramic in the toughened laminate system of natural seashell [10,11]. Returning an internally damaged composite to the superalloy operating temperature, the bridges contract via the shape memory effect providing a crack clamping force to promote diffusional rewelding of cracks as a biomimetic self-healing mechanism. Thermodynamic compatibility demands that the BCC(α) and FCC (γ) alloys be in near-equilibrium with each other at hot working and solution treatment temperatures, and that the two 2-phase α+B2 and $\gamma+\gamma'$ alloys reside in an equilibrium 4-phase α+B2+$\gamma+\gamma'$ field at service temperatures. Matrix/reinforcement interfacial strength must be limited to promote crack bridging behavior, and the austenitic alloy must exhibit higher creep strength than the ferritic alloy to maintain crack clamping forces for damage healing.

The original conceptual design and preliminary feasibility calculations by an undergraduate Materials Design class project team won 2nd prize in the first TMS-AIME national student design competition [36]. Under AASERT support, the doctoral research of B. Files has investigated the realization of this concept, taking advantage of design data being generated under a ferritic superalloy project supported by EPRI. Work so far has emphasized refinement of thermodynamic models of the Fe-Ni-Al-Ti-Co-Mo system with explicit treatment of order/disorder transitions underlying miscibility gaps. The models have identified a suitable 4-phase α-B2-γ-γ' field at a service temperature of 600C in the basic Fe-Ni-Al-Ti system, as denoted by the solid points bounding the tie-tetrahedron represented within the composition tetrahedron of Figure 15. The alloy compositions denoted A and B in the figure correspond to α+B2 and $\gamma+\gamma'$ alloys with dispersion fractions of 20%. Based on a preliminary thermodynamic database, diffusion couples of A and B type alloys were prepared and reacted 24hrs at 1100C to investigate the diffusional interaction at solution temperatures where each alloy should be single-phase. The electron microanalysis data of Figure 16 (employing a Hitachi S-4500 FEG-SEM) demonstrates a sufficiently large diffusion distance of 50-100μm allowing accurate measurement of multicomponent diffusion composition trajectories. The larger diffusion distance of Al is consistent with its predicted higher diffusivity. The measured trajectories are represented in Figure 17, projected on the median Ti plane (3.3Ti) in (a) and the median Al plane (2.5Al) in (b). The S-shaped trajectory in (a) reflects the effect of the high Al diffusivity. Also represented are

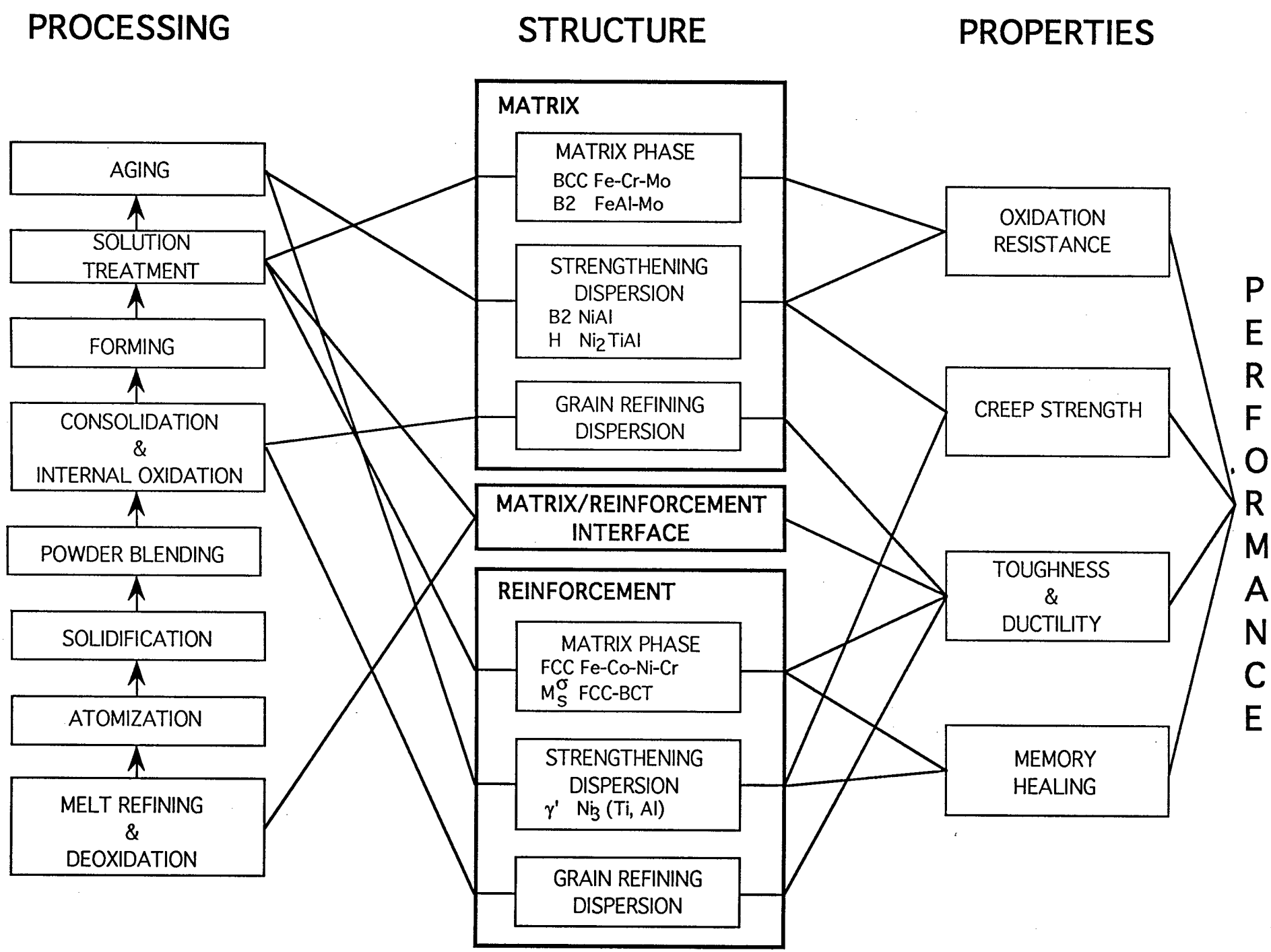

Figure 14. System structure of self-healing "smart steel" superalloy composite.

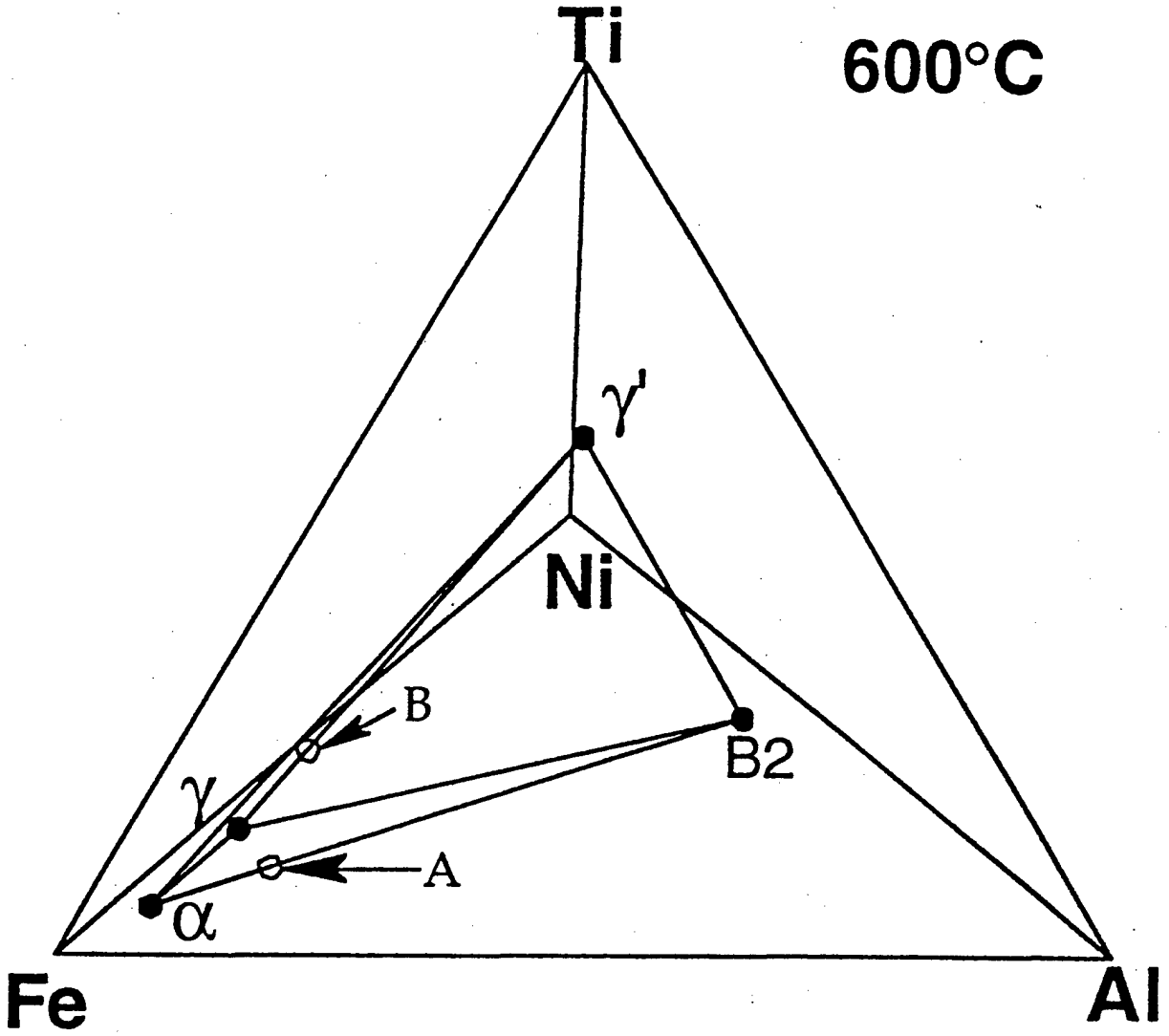

Figure 15. Computed 4-phase α-B2-γ-γ' field in Fe-Ni-Al-Ti system at 600C based on preliminary thermodynamic database. Compositions A and B represent α-B2 and γ-γ' alloys, respectively.

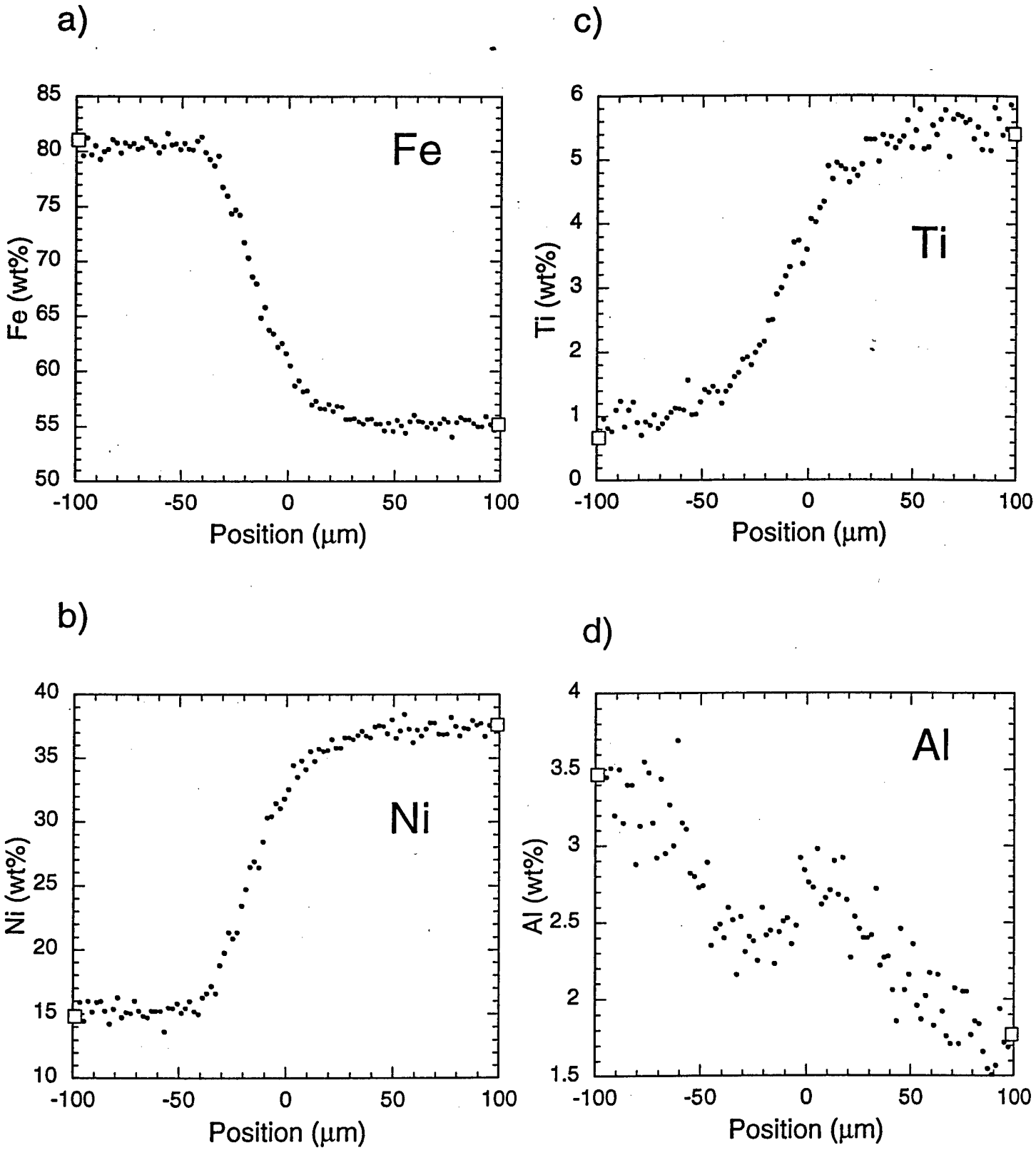

Figure 16. Measured composition profiles in diffusion couple of alloys A and B reacted 24hr at 1100C. Boxes denote bulk compositions measured far from couple interface.

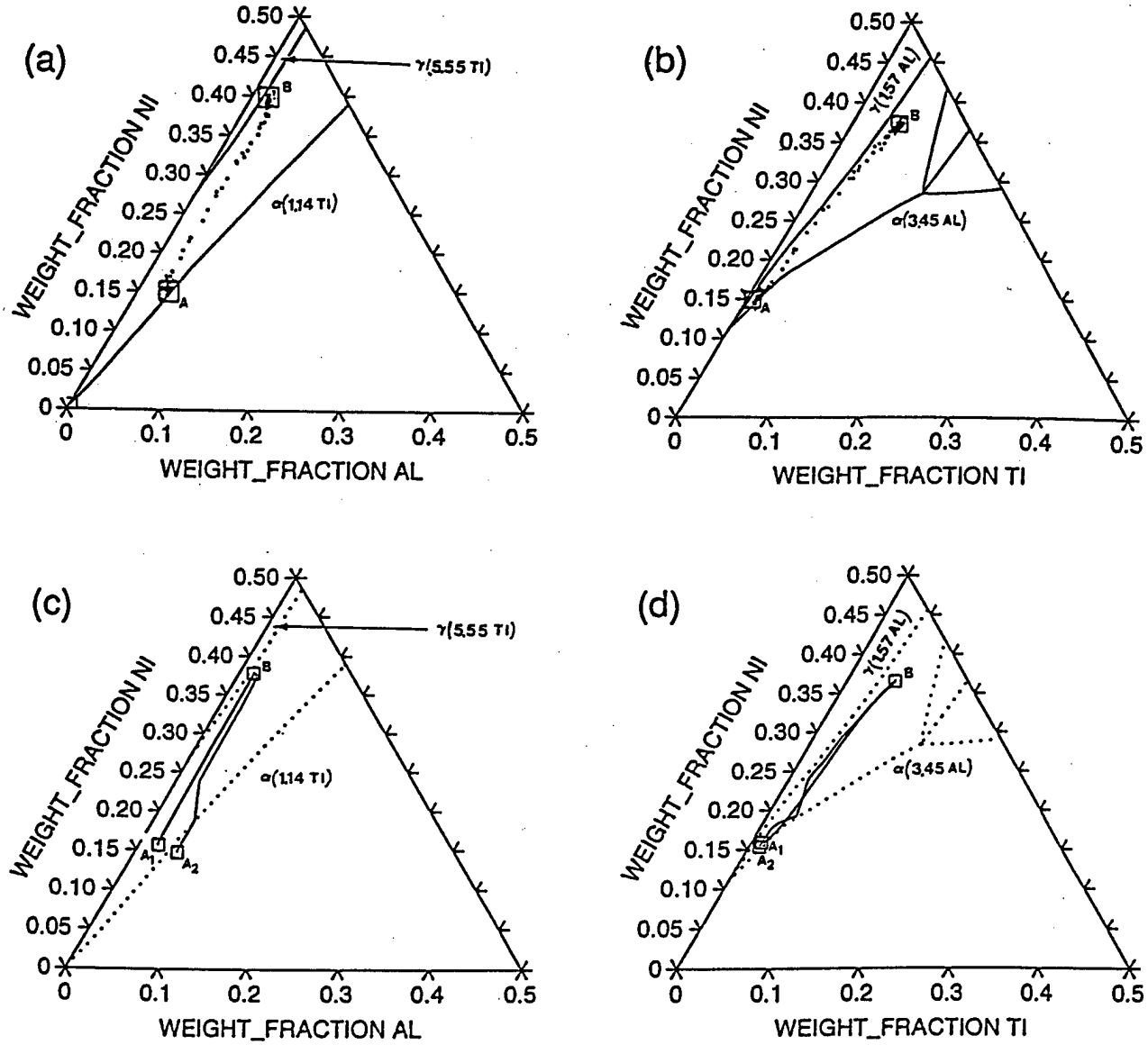

Figure 17. Measured diffusion composition trajectories in A-B couples projected on median Ti plane in (a) and median Al plane in (b). Corresponding DICTRA simulations for γ single-phase A1/B and α-γ two-phase A2/B couples in (c) and (d).

the computed boundaries of the single phase fields at the respective Ti and Al contents of alloys A and B, generated from our current database. These newer calculations indicate that alloy A is actually well within the two-phase $\alpha+\gamma$ field at 1100C. To simulate a couple between two single-phase alloys, DICTRA simulations were run modifying the A composition to the nearby single-phase α composition A2 giving the A2/B trajectories represented in (c) and (d). The "doglegs" in these projected trajectories reflect tie-lines crossing the $\gamma+\alpha$ two-phase field. Consistent with the absence of this feature in the experimental trajectories (and the lack of corresponding interface steps in Figure 16) microscopy revealed a martensitic structure in alloy A indicating the alloy was fully austenitic at 1100C. A DICTRA simulation of the interdiffusion of such a γ/γ couple is represented by that for nearby austenitic alloy A1 in (c) and (d). These preliminary couple experiments provide important input for refining the thermodynamic database to properly position the relatively narrow $\gamma+\alpha$ field in the region of interest, while also providing useful diffusivity information for further refinement of the DICTRA mobility database.

Electron micrographs in Figure 18 show that the microstructure of alloy A after aging 1 week at 600C exhibits a three-phase α+B2+γ structure with ~1 μm γ particles shown in (a). The higher magnification dark field micrograph in (b) using a 100 B2 superlattice reflection shows the desired fine dispersion of coherent B2 in the α matrix. The presence of γ at 600C in this alloy, intended to be two-phase α+B2, is in line with the finding at 1100C that the current thermodynamic database underestimates the stability of γ in this system. Further microanalysis of phase compositions will provide valuable information for refinement of the thermodynamics.

In parallel with the study of the Fe base alloys, a prototype system for testing bridging and healing concepts is being investigated mechanically using a low melting Sn-Bi alloy reinforced by TiNi shape memory alloy fibers. Blunt notch tensile specimens are employed to investigate internal cracking and healing behaviors. Experimental procedures thus developed will ultimately be applied to the Fe-base composites.

(a)

(b)

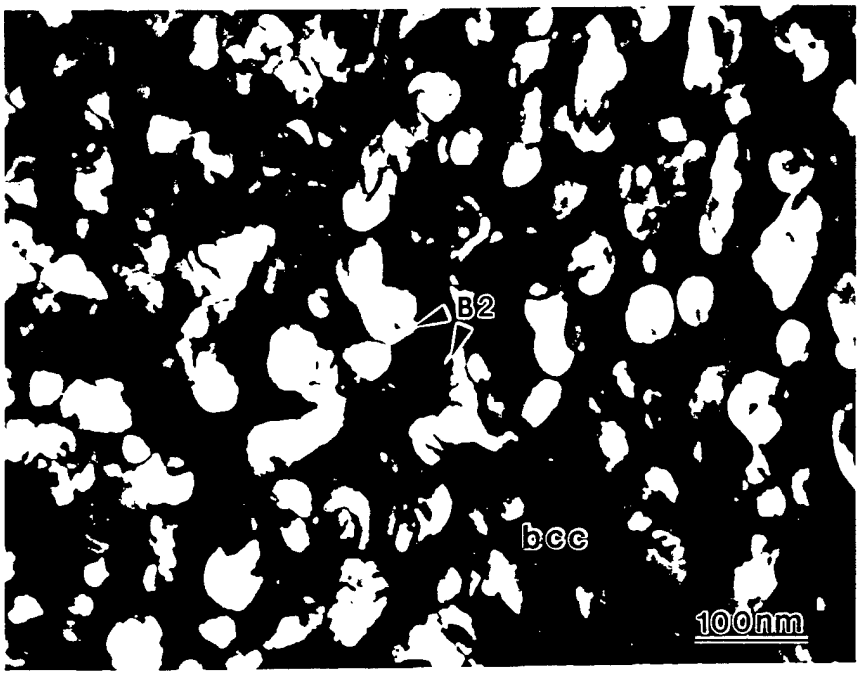

Figure 18. Electron micrographs of alloy A after aging 1 week at 600C; (a) bright field image of large γ particles in fine α-B2 matrix; (b) higher magnification dark field image using 100 B2 super-lattice reflection to reveal fine B2 dispersion in α.

C. Publications and Technical Reports

A Umantsev and G. B. Olson, "Ostwald Ripening in Multicomponent Alloys," Scripta Metall. Vol. 29 (1993) pp. 1135-1140.

C. J. Kuehmann, J. Cho, T. A. Stephenson, and G. B. Olson, "Systems Design of High Performance Steels," Metallic Materials for Lightweight Applications (40th Sagamore Army Materials Research Conference), eds. E. B. Kula and M. G. H. Wells, U.S. Government Printing Office, Washington, DC, Lake George, NY (1994) 337-355.

C. J. Kuehmann, G. B. Olson, "Computer-Aided Systems Design of Advanced Steels," Proc. International Symposium of Phase Transformations During the Thermal/Mechanical Processing of Steel - Honoring Professor Jack Kirkaldy, E. B. Hawbolt et al., eds., Metallurgical Society of the Canadian Institute of Mining, Metallurgy and Petroleum, Vancouver BC (1995) 345-356.

G. B. Olson, "Materials Design: Building a Better Martensite," to appear in Proc. C. M. Wayman International Conference on Displacive Phase Transformations and Their Applications in Materials Engineering, May 8-9, 1996, TMS-AIME.

C. J. Kuehmann and P. W. Voorhees, "Ostwald Ripening in Ternary Alloys," Met. Trans. A, 27A (1996) 937-943.

C. A. Knepfler, K. T. Faber, J. Weertman, G. B. Olson, C. R. Hubbard, O. B. Cavin, N. Packen, "High Temperature Stability and Thermal Expansion Behavior of Molybdenum-Chromium M_2C Carbides," J. Alloys & Compounds, in press.

D. Participating Scientific Personnel

Prof. Gregory B. Olson, Principle Investigator
Prof. Toshio Mura, Co-Investigator
Dr. Gautam Ghosh, Research Assistant Professor
Dr. Thomas J. Kinkus, Research Associate
Dr. Hossein Shodja, Research Associate
Dr. Alexander Umantsev, Research Associate
Shegiru Endo, Visiting Scientist
David Bergstrom, Research Assistant, Ph.D. 1995
Scott Danielson, Research Assistant, M.S./MMM 1995
Cynthia Hsieh, Research Assistant, M.S. 1994
Cheryl Knepfler, Research Assistant, Ph.D. 1994
Charles J. Kuehmann, Research Assistant, Ph.D. 1994
Ruoh-Huei Liarng, Research Assistant, Ph.D.
Henry Lippard, Research Assistant
Andrew McGeorge, Research Assistant, M.S. 1996
John Wise, Research Assistant

5. Report of Inventions

none

6. Bibliography

(*denotes papers acknowledging ARO support)

1. C. S. Smith, A Search for Structure, (1981) MIT Press: Cambridge MA

* 2. G.B. Olson, "Science of Steel," in Innovations in Ultrahigh-Strength Steel Technology, ed. G.B. Olson, M. Azrin, and E.S. Wright, Sagamore Army Materials Research Conference Proceedings: 34th (1990) 3-66.

* 3. G.B. Olson, "Materials Design: An Undergraduate Course," Morris E. Fine Symposium, eds. P.K. Liaw, J.R. Weertman, H.L. Markus, and J.S. Santner, TMS-AIME Warrendale, PA (1991) pp. 41-48.

4. C. J. Kuehmann and G. B. Olson, "Computer-Aided Systems Design of Advanced Steels," Proc. International Symposium of Phase Transformations During the Thermal/Mechanical Processing of Steel - Honoring Professor Jack Kirkaldy, E. B. Hawbolt et al., eds., Metallurgical Society of the Canadian Institute of Mining, Metallurgy and Petroleum, Vancouver BC (1995) 345-356.

5. T. A. Stephenson, C. E. Campbell, and G. B. Olson, "Systems Design of Advanced Bearing Steels," in Advanced Earth-to-Orbit Propulsion Technology 1992, eds. R. J. Richmond and S. T. Wu, NASA Conf. Pub. 3174, Vol. II (1992) pp. 299-307.

6. B. Sundman, B. Jansson and J. O. Andersson, "THERMOCALC: a Thermochemical Databank and Software System," CALPHAD 9 (1985) 153.

7. G. B. Olson, Materials Design Initiative, Dept. Materials Science and Engineering, Northwestern University, Evanston, IL.

8. C. S. Smith, "A History of Martensite: Early Ideas on the Structure of Steel," in Martensite, eds. G. B. Olson and W. S. Owen, ASM: Materials Park, OH (1992) pp. 11-20.

9. G. B. Olson and H. Hartman, "Martensite and Life: Displacive Transformations as Biological Processes," J. de Physique 43 (1982) C4-855.

10. M. Sarikaya and I. A. Aksay, "An Introduction to Biomimetics: A Structural Viewpoint," J. Mater. Sci. (1993).

11. M. Sarikaya and I. A. Aksay, "Nacre of Abalone Shell: a Natural Multifunctional Nanolaminated Ceramic-Polymer Composite Material," in Results and Problems in Cell Differentiation, ed. S. T. Case, Springer-Verlag: Berlin (1992) pp. 1-26.

12. G. R. Speich, "Secondary Hardening Ultrahigh-Strength Steel," in Innovations in Ultrahigh Strength Steel Technology, eds. G. B. Olson, M. Azrin and E. S. Wright, Sagamore Army Materials Research Conf. Proc.: 34th (1990) pp. 89-112.

* 13 J. S. Montgomery and G. B. Olson, "M_2C Carbide precipitation in AF1410," in Gilbert R. Speich Symp. Proc.: Fundamentals of Aging and Tempering in Bainitic and Martensitic Steel Products, eds. G. Krauss and P. E. Repas, ISS-AIME: Warrendale, PA (1992) pp. 177-214.

14. A. J. Allen, D. Gavillet and J. R. Weertman, "SANS and TEM Studies of Isothermal M_2C Carbide Precipitation in Ultrahigh Strength AF1410 Steels," Acta Metall. 41 (1993) 1869.

15. J. S. Langer and A. J. Schwartz, Phys. Rev. A21 (1980) 948.

16. R. Wagner and R. Kampmann, "Solid State Precipitation at High Supersaturations," in Innovations in Ultrahigh Strength Steel Technology, eds. G. B. Olson, M. Azrin and E. S. Wright, Sagamore Army Materials Research Conf. Proc.: 34th (1990) pp. 209-222.

* 17. K. C. King, P. W. Voorhees and G. B. Olson, "Solute Distribution Around a Coherent Precipitate in a Multicomponent Alloy," Metall. Trans. A 22A (1991) 2199-2210.

* 18. K. C. King, G. B. Olson and T. Mura, "Elastic Energy of Coherent Precipitation at Dislocations in an Anisotropic Matrix," Proc. ARO Workshop, Modern Theory of Anisotropic Elasticity and Applications, Ed. J. J. Wu, T. C. T. Ting, and D. M. Barnett, SIAM: Philadelphia, PA (1991) pp. 103-121.

* 19. C. J. Kuehmann and P. W. Voorhees, "Ostwald Ripening in Ternary Alloys," Met. Trans. A, 27A (1996) 937-943.

* 20. A Umantsev and G. B. Olson, "Ostwald Ripening in Multicomponent Alloys," Scripta Metall. Vol. 29 (1993) pp. 1135-1140.

21. C. Knepfler, "Synthesis and Characterization of Molybdenum-Based M_2C Carbides," Ph.D. thesis, Northwestern University Dept. Materials Science and Engineering, December, 1994.

22. A. Needleman, "A Numerical Study of Void Nucleation at Carbides," in Innovations in Ultrahigh-Strength Steel Technology, G. B. Olson, M. Azrin and E. S. Wright, eds., Sagamore Army Materials Research Conf. Proc.: 34th (1990) p. 331.

23. J. W. Hutchinson and V. Tvergaard, "Effect of Particle-Void Interaction on Void Growth in Tension and Shear," in Innovations in Ultrahigh-Strength Steel Technology, G. B. Olson, M. Azrin and E. S. Wright, eds., Sagamore Army Materials Research Conf. Proc.: 34th (1990) p. 347.

24. J. G. Cowie, M. Azrin and G. B. Olson, "Microvoid Formation During Shear Deformation of Ultrahigh-Strength Steels," Metall. Trans. A. 20A (1989) 143.

25. M. J. Gore, G. B. Olson and M. Cohen, "Grain-Refining Dispersions and Properties in Ultrahigh-Strength Steels," in Innovations in Ultrahigh Strength Steel Technology, eds. G. B. Olson, M. Azrin and E. S. Wright, Sagamore Army Materials Research Conf. Proc.: 34th (1990) pp. 425-442.

26. G. N. Haidemenopoulos, G. B. Olson, and M. Cohen, "Dispersed-Phase Transformation Toughening in Ultrahigh-Strength Steels," in Innovations in Ultrahigh Strength Steel Technology, eds. G. B. Olson, M. Azrin and E. S. Wright, Sagamore Army Materials Research Conf. Proc.: 34th (1990) pp. 549-596.

27. G.N. Haidemenopoulos, G.B. Olson, M. Cohen, and K. Tsuzaki, "Transformation Plasticity of Retained Austenite in Stage I Tempered Martensitic Steels," Scripta Metall. 23 (1989) 207-211.

28. D. Spaulding, G. B. Olson and Y-W. Chung, "Grain Boundary Cohesion and Segregation in Ultrahigh Strength Steels," submitted to Metall. Mater. Trans. A.

* 29. C. J. Kuehmann, J. Cho, T. A. Stephenson, and G. B. Olson, "Systems Design of High Performance Steels," Metallic Materials for Lightweight Applications (40th Sagamore Army Materials Research Conference), eds. E. B. Kula and M. G. H. Wells, U.S. Government Printing Office, Washington, DC, Lake George, NY (1994) 337-355.

30. C-C. Young, "Transformation Toughening in Phosphocarbide-Strengthened Austenitic Steels," Ph.D. Thesis, MIT Dept. Materials Science and Engineering, June 1988.

31. F. Stavehaug, "Transformation Toughening of γ' Strengthened Metastable Austenite Steels," Ph.D. Thesis, MIT Dept. Materials Science and Engineering, June, 1990.

32. D. Bergstrom, "Transformation Toughening in UHS Austenitic Steels," Ph.D. thesis, Northwestern University Dept. of Materials Science and Engineering, June, 1996.

33. R. G. Stringfellow and D. M. Parks, "Strain-Induced Transformation Toughening in Metastable Austenitic Steels," in Fracture Behavior and Design of Materials and Structures, Vol. 1, Ed. D. Firrao, EMAS Ltd., Warley, U.K., p. 400.

34. S. Socrate, "Mechanics of Microvoid Nucleation and Growth in High Strength Metastable Austenitic Steels", Ph.D. thesis, MIT, March, 1995.

35. D. Cook and G. Lewis, "High Performance Secondary-Hardening Gear Steel Design and Evaluation: The C2 Prototype," MSc C90 Materials Design project report, Northwestern University, June, 1994.

36. E. Chu, D. Fong, C. Klapperich and T. Yeh, "Terminator 3: Biomimetic Smart Steels," MSc C90 Materials Design project report, Northwestern University, June, 1993.

APPENDIX

Austenite Stability and Mechanical Properties of Austempered Ductile Iron

Abstract

The stability of austenite in Austempered Ductile Iron (ADI) has been quantified by measurement of the M_s^{σ} temperature, below which stress-assisted martensitic transformation controls yielding. In both the Grade 1 (115 ksi (800 MPa) yield stress) and Grade 3 (150 ksi (1030 MPa) yield stress), the M_s^{σ} temperature in uniaxial tension is near 100°C. Below this temperature the tensile yield stress shows a nonmonotonic temperature dependence indicative of isothermal martensitic transformation. Consistent with the usual stress-state sensitivity associated with the transformation dilatation, blunt notch tensile specimens with a stress-state ratio of $\Sigma = \sigma_h / \bar{\sigma} = 1.1$ demonstrate an increased M_s^{σ} near 190°C. From these stability measurements it is estimated that the temperature of maximum transformation toughening, corresponding to the M_s^{σ} for a crack-tip stress state of $\Sigma \approx 2.3$, would be greater than 300°C. Below room temperature the measured temperature dependence of the fracture toughness is dominated by the ductile / brittle transition, and it is obscured at higher temperatures by the high scatter associated with the distribution of graphite nodules. Although clear metallographic support could not be obtained, the measured stability indicates that the austenite should transform during fracture, but the stability is too low to give significant transformation toughening. Higher toughness at and above room temperature should then be

achievable by increasing austenite stability. However, the measured stress-strain curve shapes are consistent with a broad distribution of austenite stabilities, as indicated by the lack of sharp yielding at low temperatures. This suggests that the stabilities measured in this work represent the least stable austenite in the distribution, and that the breadth of the distribution limits the transformation toughening. The stress-strain curves also indicate enhanced strain hardening at temperatures above 200°C from possible stress-assisted bainitic transformation.

Introduction

Several investigations have shown that austempered ductile irons exhibit improved mechanical properties compared to conventional cast irons [1-5]. Much of their favorable combination of strength and ductility can be attributed to the presence of a significant amount of retained austenite. The stability of this austenite with respect to the formation of mechanically induced martensite depends sensitively on its carbon content, which can change significantly with slight changes in austempering time or temperature [6]. If the austenite stability could be optimized, the mechanical properties could be improved even more by the process of transformation toughening. It is well known that mechanically induced martensitic transformations can enhance ductility and fracture toughness if the austenite is of the proper stability [7]. This stability is quantified by the M_S^{σ} temperature. Defined as the temperature below which initial yielding is due to martensitic transformation, the M_S^{σ} is a strong function of the imposed stress state. Experimentally M_S^{σ} is determined as the temperature at which the temperature dependence of the measured yield stress reverses. The present study has been undertaken to determine the M_S^{σ} temperatures under different stress states and assess

the effect of transformation plasticity on the mechanical properties in two grades of an austempered ductile iron.

Materials and Procedures

One inch and half inch thick plates of ADI of weight percent composition, 3.7 C, 2.7 Si, 0.97 Ni, 0.87 Cu, 0.27 Mn, 0.057 Mg and 0.032 Cr, were received from the U.S. Army Research Laboratory Materials Directorate. The material had been heat treated according to ASTM standard A 897-90 [8] to produce at least one plate each of Grades 1 and 3 for both thicknesses. The heat treatments used are listed in Table 1. Uniaxial and blunt notched tensile tests and K_{IC} fracture toughness tests were performed at temperatures from -196°C to 350°C in order to determine the effect of austenite stability and stress state on the flow behavior and fracture toughness of these materials.

	Grade 1	Grade 3
Preheat Time & Temp.	105 min at 593°C (1100°F)	120 min at 593°C (1100°F)
Austenitizing Time & Temp.	100 min at 891°C (1635°F)	150 min at 885°C (1625°F)
Quench Time & Temp.	100 min at 327°C (620°F)	150 min at 316°C (600°F)
Quench Medium	Molten Salt	Molten Salt
Rockwell C Hardness	32.2	41.5

Table 1 Heat treatments applied to produce plates of Grades 1 and 3.

In the initial stages of this work, seventeen tensile specimens were made from each of the half-inch plates, in order to measure their uniaxial tension M_S^{σ} temperatures. Tensile tests were performed at temperatures from -196°C to 236°C. Below 20°C the tests were conducted in isopentane or methanol cooled by liquid nitrogen or in pure liquid nitrogen, from 20°C to 150°C they were conducted in air and above 150°C in vacuum. The tensile specimen geometry is shown in Figure 1a.

To determine how sensitive the martensitic transformation is to the triaxiality of the stress state, blunt-notched tensile specimens of the type shown in Figure 1b were made. Ten specimens were made from Grade 1, and five were made from Grade 3. They were strained to failure at temperatures from -196°C to 225°C in the same environments that were used for the uniaxial tensile tests.

K_{IC} fracture toughness tests were performed according to ASTM standard E 399-89 on compact tension specimens which were cut from the half-inch plates of each grade. Tests run below 20°C were in air cooled by nitrogen, those from 20°C to 150°C were run in air and those above 150°C were tested in vacuum.

Results and Discussion

The 0.2% offset yield stress versus temperature data from the uniaxial tension tests are plotted in Figure 2. As the figure shows, both grades have a very broad peak around 100°C. Because of the peak breadth and scatter, it is difficult to determine an exact M_S^{σ}, but there appears to be little difference in stability between the two grades. Figure 2 also shows the yield stress versus temperature curves for the blunt-notch tensile tests. Once again, both grades display broad peaks. However, as expected for

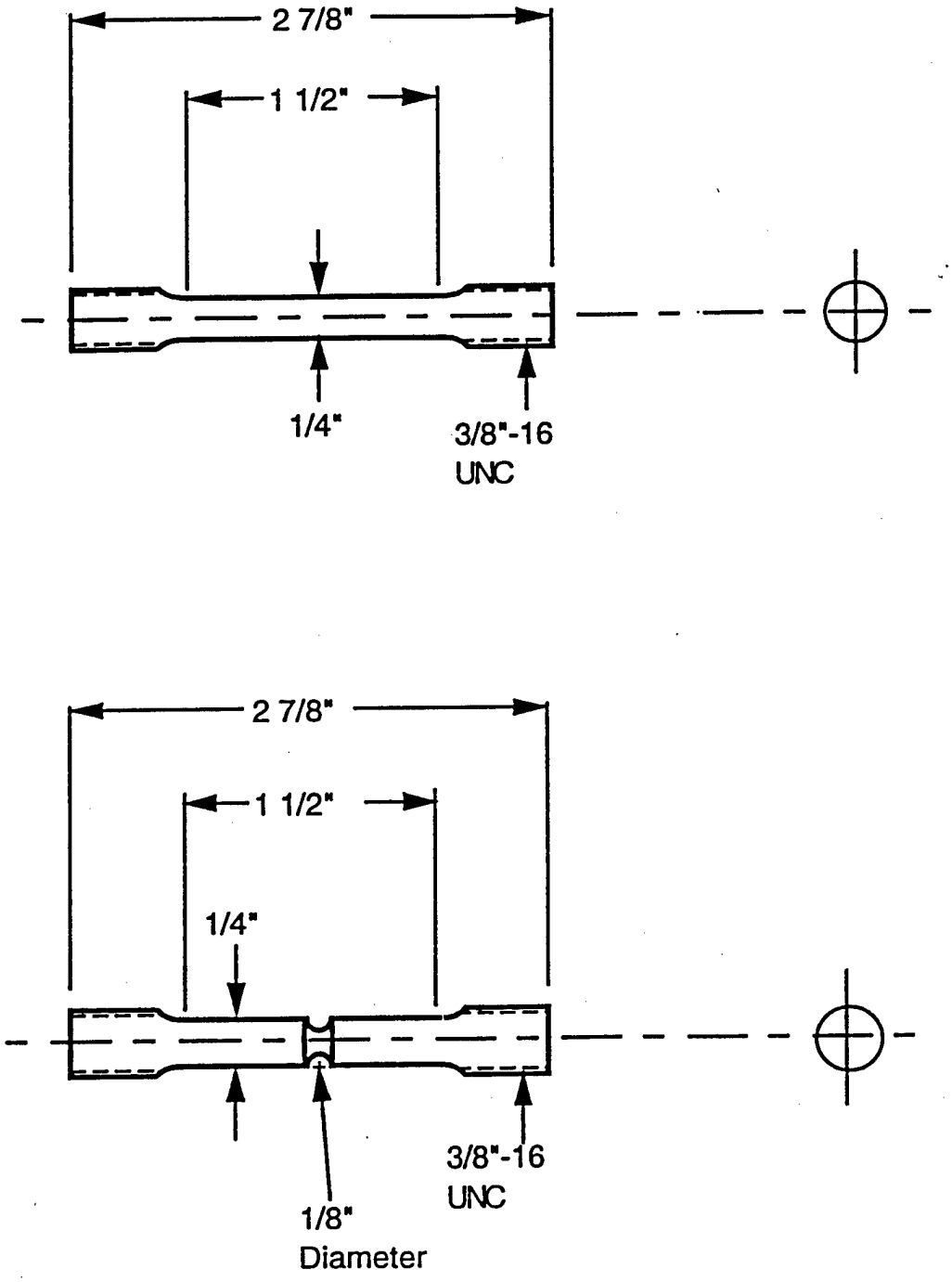

Figure 1 Uniaxial and blunt notch tensile specimens.

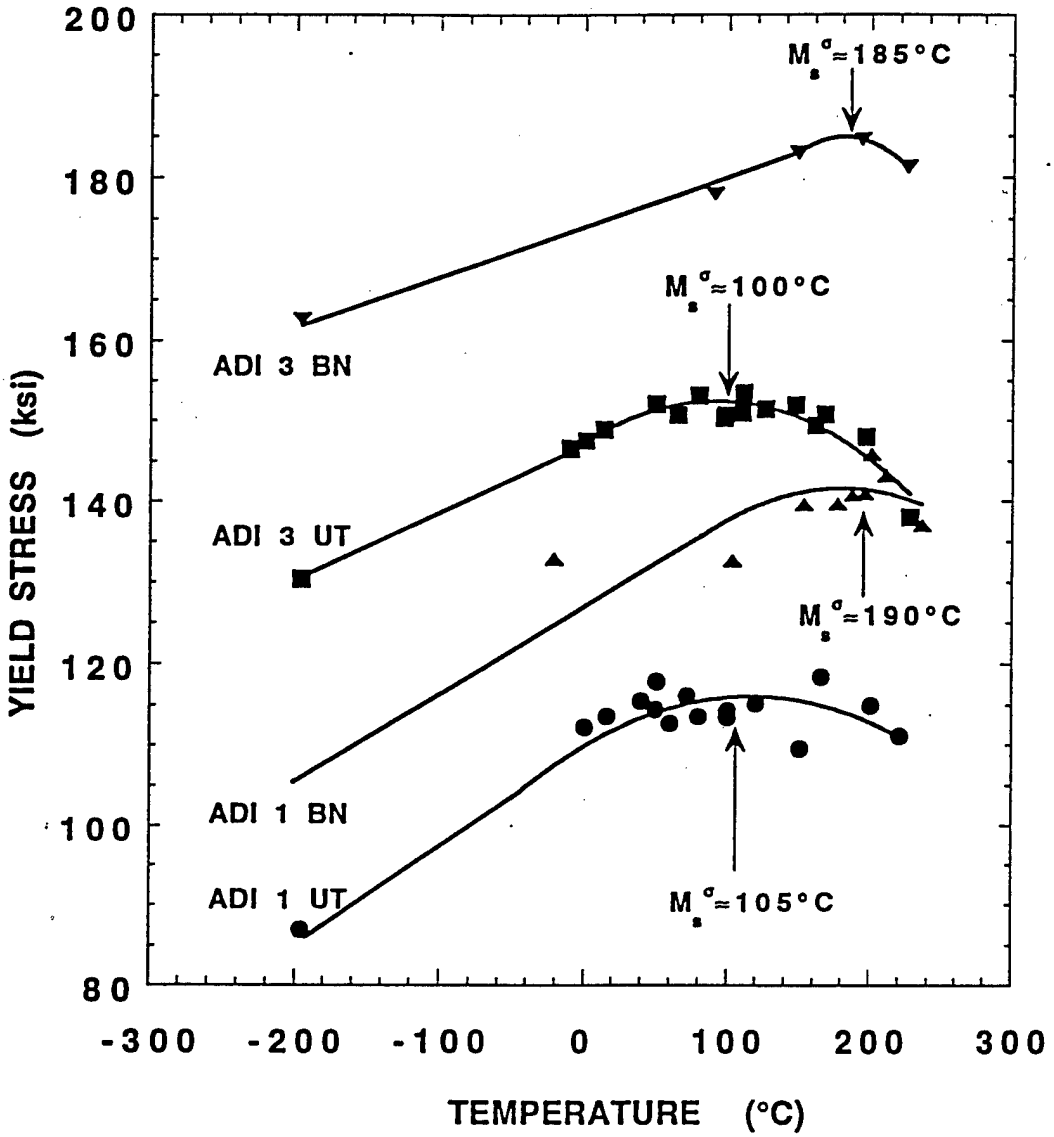

Figure 2 A plot of 0.2% yield stress versus temperature from uniaxial and blunt notch tensile tests on material from the 1/2 inch plates.

this more highly triaxial stress state, the M_S^{σ} temperatures are about 85° higher than in uniaxial tension.

Based on these observations and a parallel study by Matlock and Krauss [5], a more extensive study was made of the properties of the Grade 1 material in uniaxial tension. As this grade was shown to have nearly 10% more retained austenite [5], the effects of austenite stability on the mechanical behavior should be more apparent than in the Grade 3 material. Figure 3 shows the 0.2% yield stress, UTS and fracture strain of Grade 1 material from the 1 inch plate at temperatures from -196°C to 350°C, while Figure 4 shows stress-strain curves from these tests at selected temperatures.

The dip in 0.2% yield stress at very low temperatures is evidence of isothermal martensite formation. The fact that the curves do not exhibit a sharp stress plateau after the onset of transformation controlled yielding indicates that there is a range of austenite compositions in this material, likely associated with a distribution in carbon content. The stabilities measured by M_S^{σ} thus represent the least stable austenite in the distribution. The inflections in the stress strain curves for tests above 200°C suggest another change in structure is taking place, most likely the formation of stress assisted bainite. The maximum fracture strain and a local maximum in UTS (which is equal to the fracture stress, since there is no appreciable necking) occur at near 250°C in the temperature regime where this transformation occurs.

K_{IC} fracture toughness tests were performed on compact tension specimens of the type shown in Figure 5, which were cut from the half inch plates of each grade. The results of these tests are shown in Figure 6. These are provisional "K_Q" values because, except at room temperature, it was not possible to use our C.O.D. gage. However, when values obtained using the gage at room temperature were compared to those

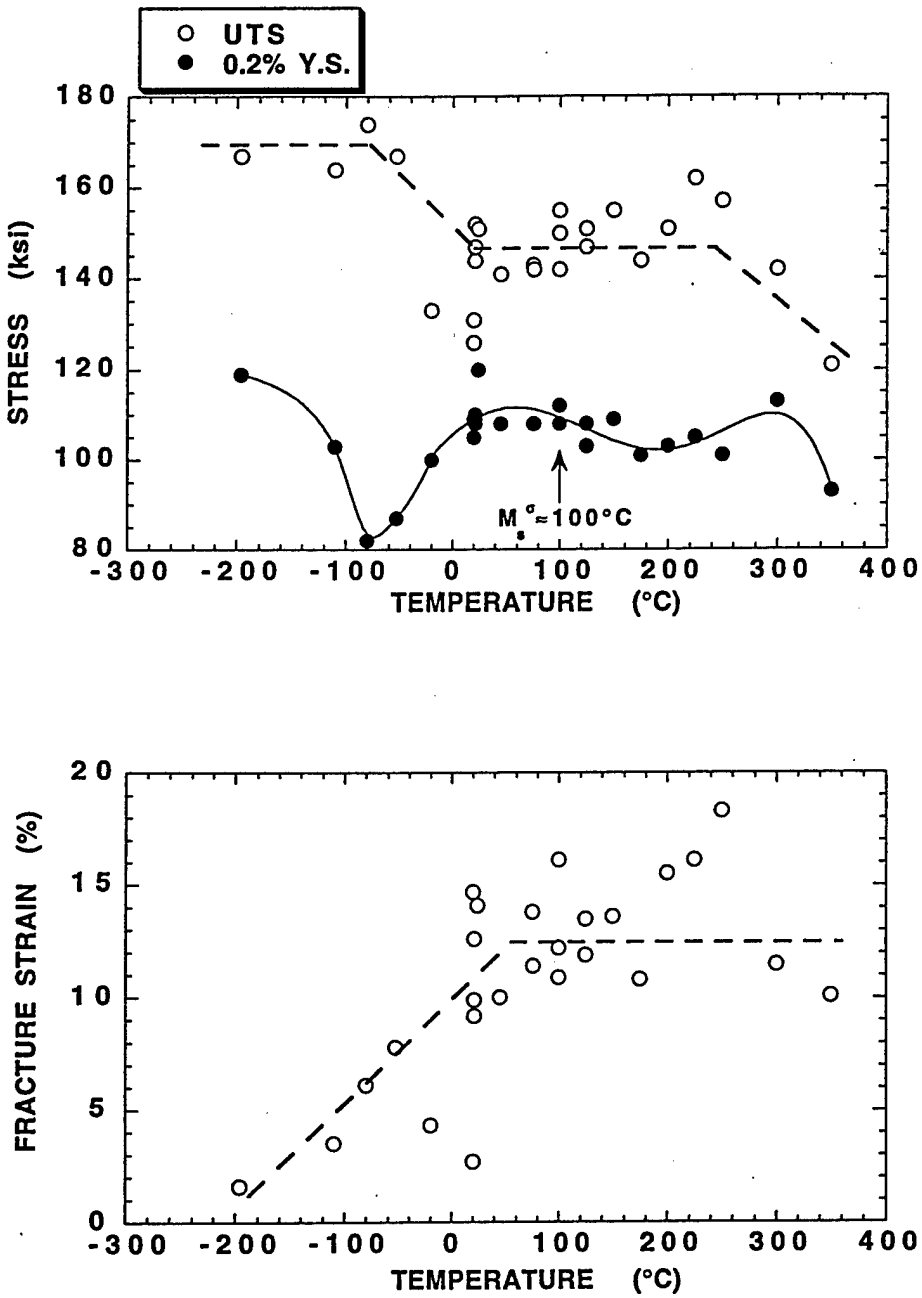

Figure 3 Plots of 0.2% yield stress and UTS (top) and fracture strain (bottom) versus temperature for Grade 1 material from the 1 inch plate.

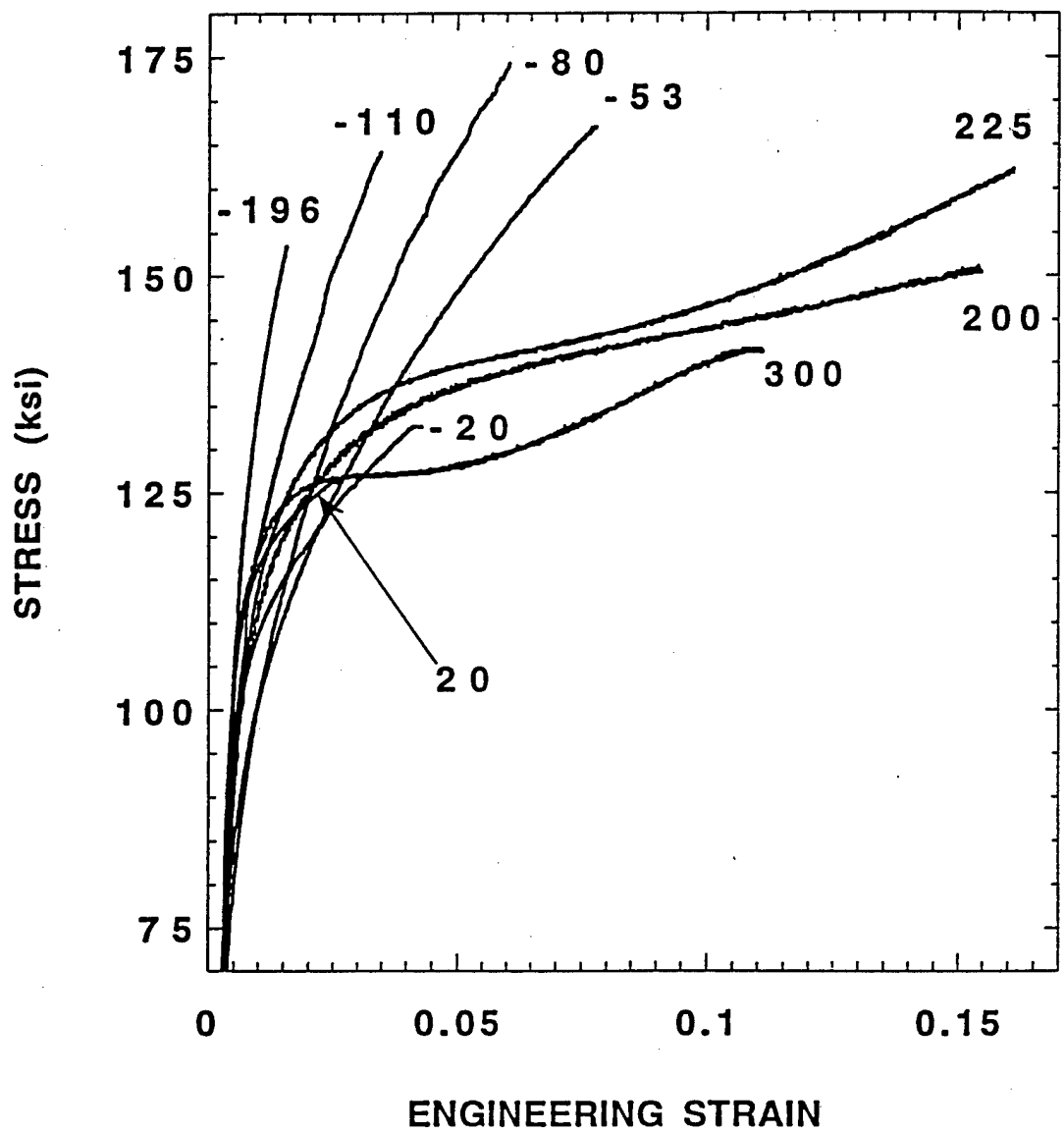

Figure 4 Stress-strain curves for Grade 1 specimens from the 1 inch plate in uniaxial tension at selected temperatures.

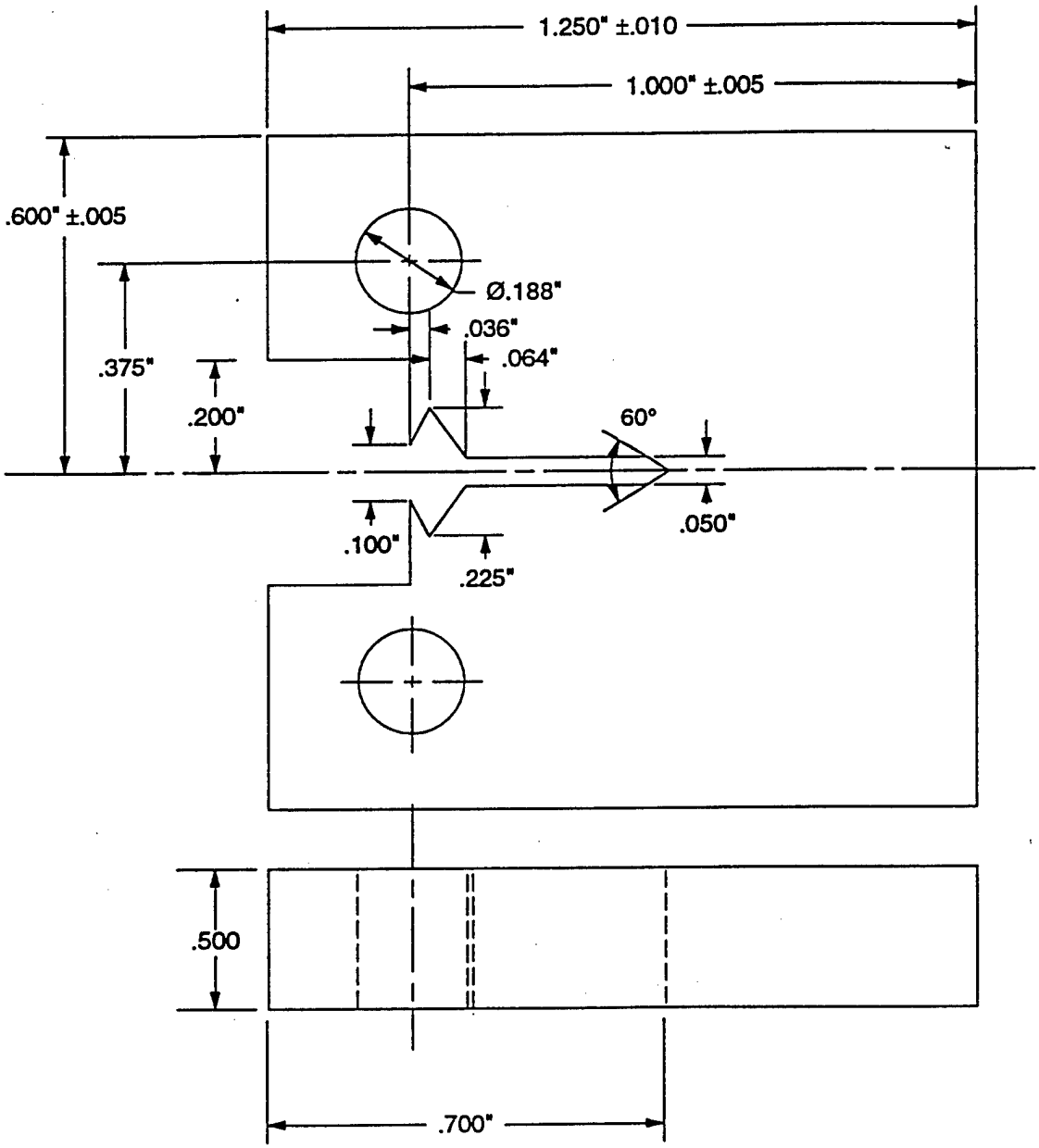

Figure 5 Compact tension fracture toughness specimen.

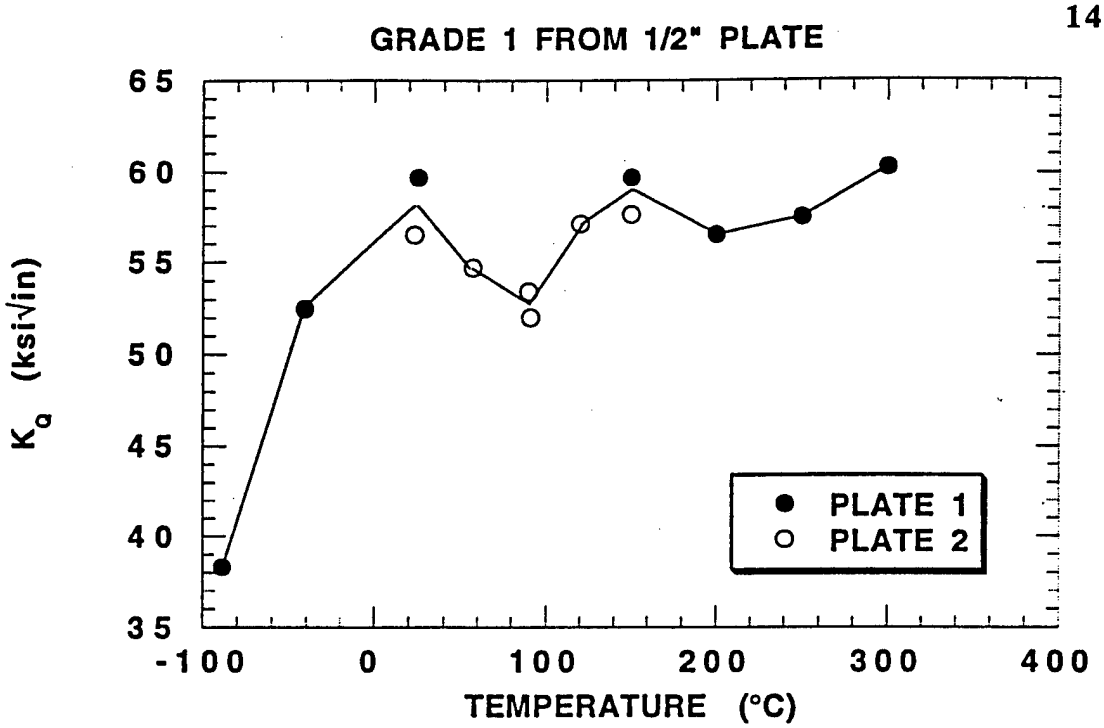

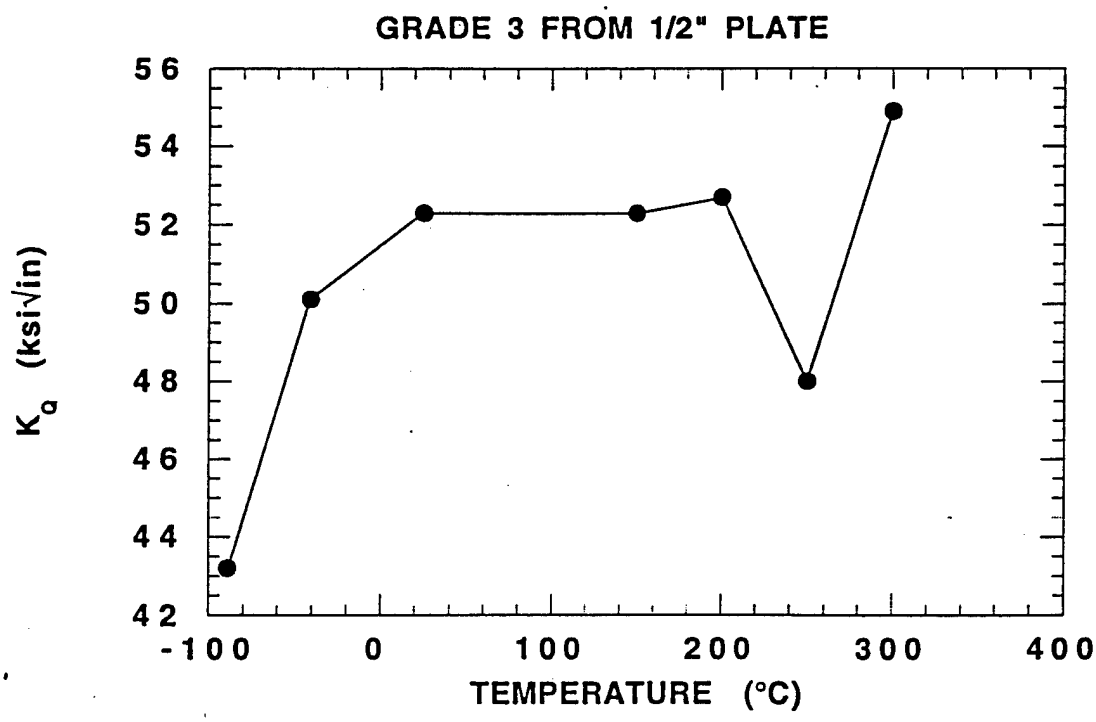

Figure 6 Plots of K_Q fracture toughness versus temperature for Grades 1 and 3 from the 1/2 inch plates.

calculated at the same temperature without using the gage, they were virtually the same. Therefore, the K_Q values should be a good approximation of K_{IC} at other temperatures.

As denoted in Figure 6a, specimens of the Grade 1 material were cut from two different plates. Although both plates were given the same heat treatment, the material from the first plate had a hardness of R_C 32 while those from the second plate measured R_C 34. Combining the data from the two plates, no clear peak in fracture toughness is evident.

The most noticeable feature of these tests is the significant embrittlement at low temperatures. As Figure 6 shows, the fracture toughness of each grade drops sharply as the temperature falls below 0°C. Between room temperature and -40°C, the fracture toughness decreases by over 10% (for Grade 1), while the uniaxial fracture strain drops by about 50% (Figure 3). Between room temperature and -80°C the fracture toughness drops by more than 30%. Above room temperature, K_Q remains relatively constant until it rises again above 250°C. Figure 7 shows the fracture surfaces of compact tension specimens tested at -90°C and 300°C. These images clearly demonstrate the change of fracture mode from ductile to brittle at low temperatures.

These tests indicate little difference in austenite stability among the grades and plate thicknesses. In uniaxial tension the M_S^{σ} temperatures were measured at about 100°C, while they were found to be near 190°C for blunt notch tension. Based on these values, the M_S^{σ} temperature for a crack-tip stress state was estimated to be in excess of 300°C. However, this could not be experimentally verified because it was too close to

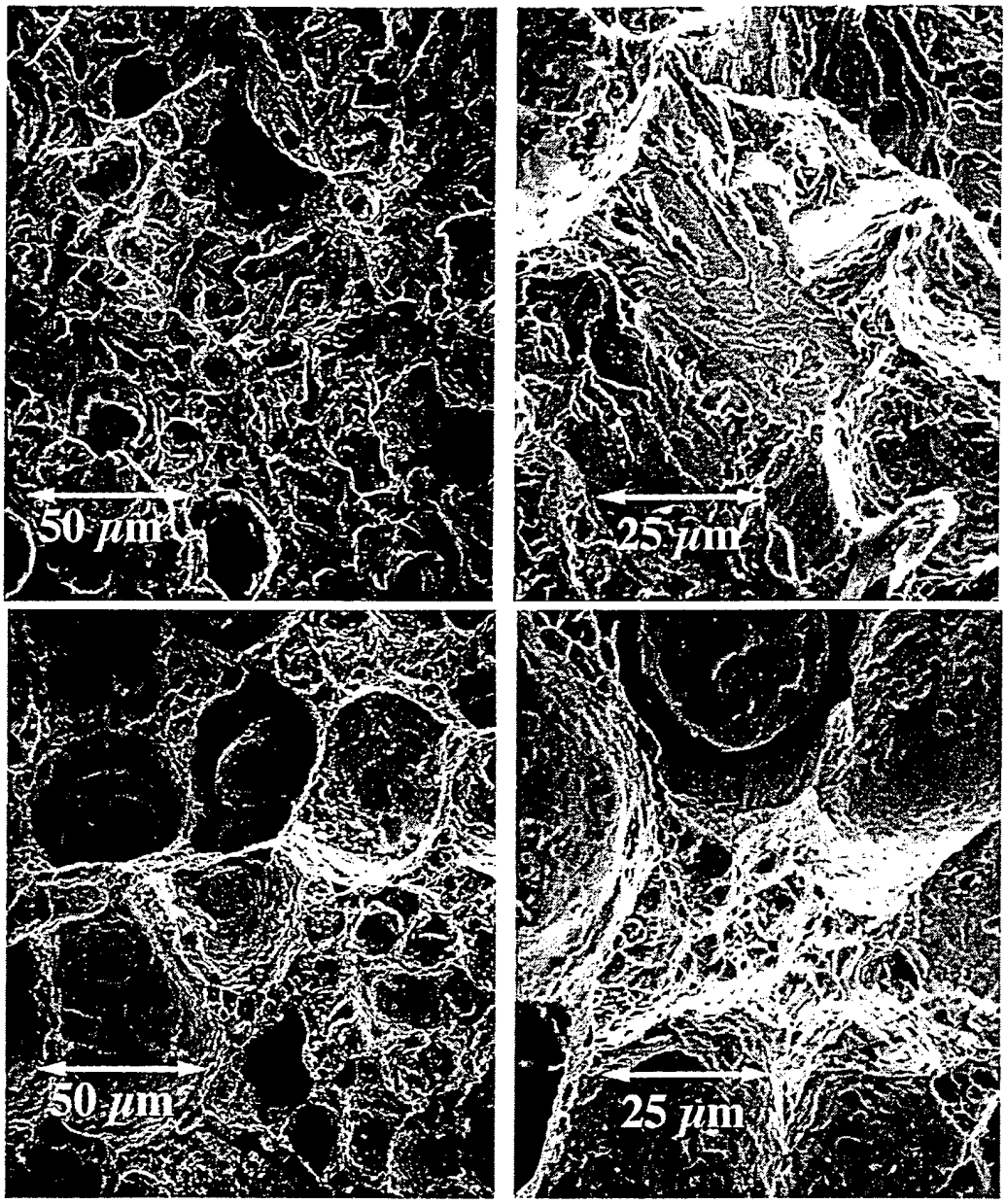

Figure 7 SEM micrographs of compact tension specimen fracture surfaces of Grade 1 material from the original 1/2 inch plate, fractured at -90°C (top) and 300°C (bottom).

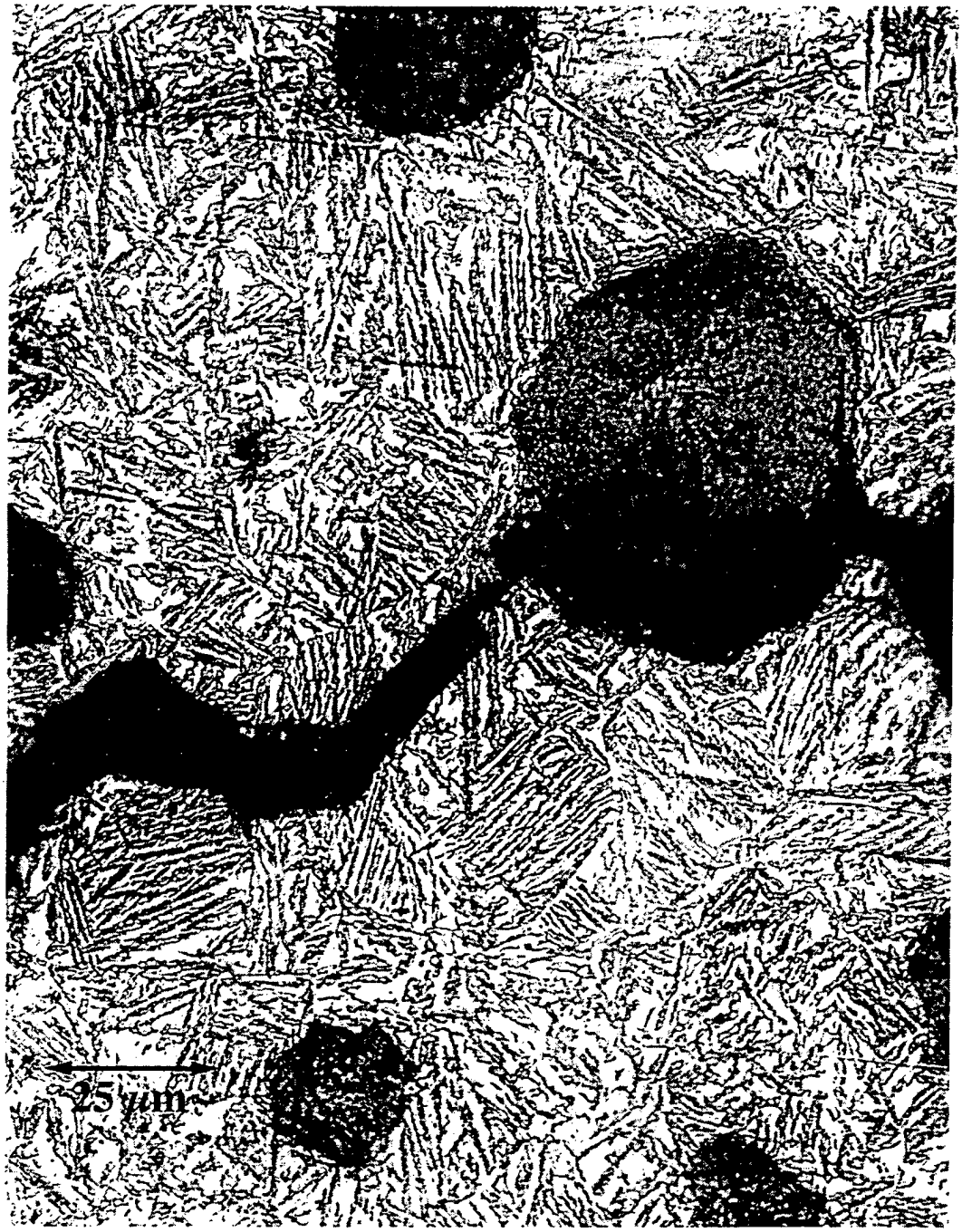

Figure 8 Optical micrograph of a uniaxial tension specimen of Grade 1 material from the 1/2 inch plate that was strained to failure at -196°C.

the austempering temperature. It should be noted again that the measured austenite stabilities likely represent the least stable of a range of compositions. It may be that this range of stabilities is too broad to show a well defined transformation toughening peak.

The presence of stress-assisted plate martensite is expected in the specimens tested below their M_S^{σ}. Several of these samples were examined using light and scanning electron microscopy in an attempt to confirm the presence of this martensite. Aranzabal *et al*. [1] saw stress-assisted martensite near a fracture surface using a 4% Nital etch, and Kovacs [9] reports that, after applying this same etchant, a four to eight hour heat tint at 500°F will cause any martensite to turn a deep blue. However, after trying both of these methods, no martensite could be distinguished, even in the specimen shown in Figure 8, which was strained to failure in liquid nitrogen.

Conclusions

The austenite stability has been measured in terms of the M_S^{σ} temperature under several states of stress for two grades of austempered ductile iron. For Grade 1 material, M_S^{σ}(UT)≈105°C and M_S^{σ}(BN)≈190°C, while M_S^{σ}(UT)≈100°C and M_S^{σ}(BN)≈185°C for Grade 3 material. Based on these measurements, M_S^{σ} (CT) was estimated to be in excess of 300°C for both grades. Although, because of the complex microstructure, conclusive metallographic evidence of martensite formation was not found, these stability measurements are consistent with the occurrence of mechanically-induced martensitic transformation. Below these temperatures, the yield stress decreases in a manner indicative of stress-assisted martensitic transformation. Above M_S^{σ}, the effect of transformation on toughness is obscured by scatter due to the large volume fraction of graphite particles and the likelihood that compositional inhomogeneities

resulted in a wide distribution of austenite stabilities. At temperatures above 200°C the stress-strain curves show increased strain hardening, which may be evidence of stress-assisted bainite formation.

Below 20°C, both grades pass through the ductile to brittle transformation temperature and their toughness and ductility drop rapidly.

Acknowledgments

The author would like to thank the U. S. Army Research Laboratory for sponsorship of this work and Dr. Martin G. H. Wells of ARL for his assistance.

Appendix References

1. J. Aranzabal, I. Gutierrez, J.M. Rodriguez-Ibabe, and J.J. Urcola, "Influence of Heat Treatments on Microstructure and Toughness of Austempered Ductile Iron," *Mat. Sci. and Tech.*, **8** (1992) 263-73.

2. K.B. Rundman, D.J. Moore, K.L. Hayrynen, W.J. Dubensky and T.N. Rouns, "The Microstructure and Mechanical Properties of Austempered Ductile Iron," *J. Heat Treat.*, **5** (1988) 79-95.

3. N. Darwish and R. Elliot, "Austempering of Low Manganese Ductile Irons," *Mater. Sci. Technol.*, **9** (1993) 572-585.

4. B.V. Kovacs, "Austempered Ductile Iron: Fact and Fiction," *Modern Casting*, **90** (1990) 38-41.

5. D.K. Matlock and G. Krauss, " Mechanical Performance of Austempered Ductile Iron," *Report submitted to U. S. Army Research Laboratory Materials Directorate,* December, 1993.

6. K.B. Rundman and R.C. Klug, "An X-Ray and Metallographic Study of an Austempered Ductile Cast Iron," *AFS Trans.* **91** (1983) 499-508.

7. G. B. Olson and M. Cohen, in : *Mechanical Properties and Phase Transformation in Engineering Materials*, S. D. Antolovich, R. O. Ritchie and W. W. Gerberich, eds., TMS-AIME, Warrendale, PA (1986) 367.

8. "E 897-90 : Standard Test Method for Plane-Strain Fracture Toughness of Metallic Materials," in : *1992 Annual Book of ASTM Standards, American Society for Testing and Materials*, Philadelphia, PA (1992) 557-562.

9. B.V. Kovacs, "A Simple Technique to Identify Various Phases in Austempered Ductile Iron," *Modern Casting*, **77** (1987) 34-35.